Satellite (GOSAT-2 CAI-2) retrieval and surface (ARFINET) observations of Aerosol Black Carbon over India

Mukunda M. Gogoi[1], S. Suresh Babu[1], Ryoichi Imasu[2], Makiko Hashimoto[3]

[1]Space Physics Laboratory, Vikram Sarabhai Space Centre, ISRO, Thiruvananthapuram 695-022, India
[2]Atmosphere and Ocean Research Institute, The University of Tokyo, Chiba 277-8568, Japan
[3]Space Technology Directorate I, Earth observation research centre, JAXA, Ibaraki 305-8505, Japan

Correspondence to: Mukunda M. Gogoi (mukunda.mg@gmail.com), Ryoichi Imasu (imasu@aori.u-tokyo.ac.jp)

Abstract. The light-absorbing Black Carbon (BC) aerosols have very sensitive role in affecting the Earth's radiation budget and climate. In this study, satellite retrieval of BC over India is presented based on observations from the Cloud and Aerosol-Imager-2 (CAI-2) on-board the Greenhouse gases Observing Satellite-2 (GOSAT-2). To evaluate and validate the satellite retrievals, near surface BC mass concentrations measured across Aerosol Radiative Forcing over India NETwork (ARFINET) of aerosol observatories are used and the findings are extended to comprehend the global BC features. As the analysis reveals, this satellite retrieval clearly depicts the regional and seasonal features of BC over the Indian region, like those recorded by surface observations. The validation and closure studies between the two data sets show RMSE < 1 and absolute difference below 2 µg m^{-3} for > 60% of simultaneous observations, possessing good associations in December, January, and February (R ~ 0.73) and March, April, and May (R ~ 0.76). Over the hotspot regions of India, the satellite retrievals show soot volume fraction of ~ 5%, columnar single scattering albedo of ~ 0.8 and BC column optical depth of ~ 0.1 during the period of highest BC load; which are comparable to those of other in-situ or satellite measurements. In terms of global spatio-temporal variability, satellite retrievals show higher BC occurring mostly in areas where biomass burning is intense. Overall, this study highlights the effectiveness of satellite retrieval of BC, which could be effectively used for the regular monitoring of BC load arising out of vehicular/ industrial/ biomass burning activities across the globe.

1 Introduction

The convergence of various experimental and modeling studies on the climate warming potential of atmospheric Black Carbon (BC) necessitates its accurate quantification and seasonal source characterization at the regional and global scale (Bond et al., 2013; Gustaffson and Ramanathan, 2016; IPCC, 2021). Concerted efforts have been made to understand the radiative properties of BC (warming as well as offsetting the scattering effects of aerosols) arising out of the incomplete combustion of bio-fuel or fossil-fuel sources. Though nearly accurate estimation of BC is made using in-situ approach (uncertainty in BC measurements < 5-10%; Manoj et al., 2019), most of the studies confining to in-situ measurements (ground based or air-borne) have limited spatial coverage. Similarly, model simulated BC though have good spatio-temporal coverage are subjected to deviations from the real BC environment, mainly due to the inaccurate model inventories and meteorological input available for the simulations (Vignati et al., 2010). In this regard, retrieval of BC from satellite-based radiation measurements synchronizing with the ground-based point-measurements is a novel idea to quantify and classify the real BC environment across distinct geographic regions of the globe. However, it is challenging to accurately retrieve backscattering signal from optically thin BC aerosols lofted above highly heterogeneous land surfaces, such as vegetated, desert, semiarid and urban regions, having diverse surface reflectance properties. The complex optical properties of BC arising out of the highly heterogeneous sources and transformation processes add further complexity to the satellite retrieval, especially over the land. Even though several new algorithms have been developed for aerosol retrieval over land (e.g., Multi-Angle Imaging Spectroradiometer (MISR) retrieval by Dinner et al., 1998; Dark Target method by Levy et al., 2007; Non-linear optimal estimation algorithm for retrieval of aerosol microphysical properties from SAGE II satellite

40 observations in the volcanically unperturbed lower stratosphere by Wurl et al., (2010); Multi-Angle Implementation of Atmospheric Correction (MAIAC) by Lyapustin et al., 2011; Deep Blue aerosol retrieval algorithm by Hsu et al., 2013; UV method by Fukuda et al., 2013; Multi-Angle and Polarization Measurements of Radiations by Dubovik et al., 2011, 2014; GOCI Yonsei Aerosol Retrieval (YAER) algorithm by Choi et al., (2016); Multi-Wavelength and -Pixel Method (MWPM) by Hashimoto and Nakajima, 2017 etc.), the retrieval of BC from satellite-based radiation measurement is very limited.

45 Based on Effective Medium Approximations and statistically optimized aerosol inversion algorithm, Bao et al., (2019) have reported the retrieval of the surface mass concentration of BC from PARASOL (Polarization and Anisotropy of Reflectance for Atmospheric Sciences Coupled with Observations from a LiDAR) measurements. In another paper by Bao et al., (2020), MODIS Aqua Level-1B observations (MYD021KM) at three visible-infrared channels (470, 660, and 2100 nm) are used to estimate the columnar concentrations of BC aerosols based on BC and non-BC Maxwell−Garnett effective medium

50 approximation. POLDER/PARASOL satellite observations are also used by Li et al., (2020) to retrieve BC and brown carbon concentrations based on aerosol component approach of Li et al., (2019). Apart from satellite observations, there are also efforts to retrieve BC from ground based remote sensing data. Hara et al., (2018) have reported the retrieval of BC from multi-wavelength Mie-Raman lidar observations, based on the modified algorithm of Nishizawa et al., (2017). Ceolato et al., (2022) have reported a direct and remote technique to estimate the BC number and mass concentration from picosecond

55 short-range elastic backscatter lidar observations.

The objective of this paper is to present the regional distribution of BC over India based on satellite-based observations by Cloud and Aerosol-Imager-2 (CAI-2) on-board Greenhouse gases Observing Satellite-2 (GOSAT-2). To evaluate and validate the spatio-temporal distribution of BC from satellite retrieval, near surface BC mass concentrations measured across Aerosol Radiative Forcing over India NETwork (ARFINET; Babu et al., 2013; Gogoi et al., 2021) of aerosol observatories

60 are used and the findings are extended to comprehend the global BC features. The main purpose of CAI-2 is to derive cloud areas to improve accuracy in greenhouse gas (GHG) retrieval by Fourier Transform Spectrometer (FTS) in addition to determining the concentrations of BC mass and fine particulate matter (PM2.5) based on aerosol optical thickness of fine mode particles.

In the ARFINET, the main objective of the measurements of various aerosol parameters (e.g., columnar aerosol optical
65 depth, BC mass concentrations, etc.) is to characterize their heterogeneous properties in space, time, and spectral domains, develop periodic and accurate estimates of aerosol radiative forcing over India, and assess their impacts on regional and global climate. Since its very modest beginnings in 1985, the network has expanded to more than 40 observatories today. Supplementary Table-T1 provides more details regarding the ground-based observational locations in the ARFINET. The stations are arranged and grouped with respect their geographic positions (Fig-1) in the Indo-Gangetic Plains (IGP);

70 Northeastern India (NEI); Northwestern India (NWI); Himalayan, sub-Himalayan and foothills regions (HIM), Central India (CI), Peninsular India (PI) and Island Locations (IL). The systematic and long-term monitoring of BC in the ARFINET began in 2000, followed by gradual extension of the observational sites in phases. In this study, the use of ground-based BC from the ARFINET is unique in a way that the BC over the Indian region is highly heterogeneous, both in terms of spatial and temporal scales (Manoj et al., 2019; Gogoi et al., 2017; 2021). With rapidly growing industrial and transport sectors,

75 mixed with diverse uses of fossil and bio-fuels in the domestic and industrial sectors, the Indian region is a complex blend of emissions and atmospheric processes (Babu et al., 2013; Gogoi et al., 2021). While the shallow atmospheric boundary layer leads to very high concentrations of BC near the surface in winter (December-February), especially over the northern part of India (Nair et al., 2007; Pathak et al., 2010; Gogoi et al., 2013, Vaishya et al., 2017), the synoptic circulations and convective processes are dominant in horizontal and vertical re-distribution of BC in the pre-monsoon (March-May) and monsoon

80 (June-September) seasons (Babu et al., 2016; Nair et al., 2016; Gogoi et al., 2019, 2020). Thus, the synergistic study of the

regional BC distribution by combining satellite and surface measurements over the Indian region is unique in terms of enabling retrieval accuracy as well as expanding it to the understanding of its global distribution in near-real time.

2 Data and Methodologies

2.1 Retrieval of aerosol properties from Cloud and Aerosol Imager -2 (CAI-2)

CAI-2 on-board GOSAT-2 satellite is a push-broom imaging sensor which records the backscattered radiances at 7-wavelengths/ 10-spectral bands in ultraviolet (UV: 339, 377 nm), visible (VIS: 441, 546, 672 nm) and near-infrared (NIR: 865, 1630 nm) equipped in forward (bands: 339, 441, 672, 865 and 1630 nm) and backward (bands: 377, 546, 672, 865 and 1630 nm) looking directions (± 20°). For cloud discrimination as well as deriving aerosol properties, CAI-2 Level 1B (L1B) data is used, which contains spectral radiance data per pixel converted from sensor output (GOSAT-2 TANSO-CAI-2 L2 Pre-processing ATBD).

The flowchart of CAI-2 L2 preprocessing algorithm is shown in the supplementary Figure-S1. The radiance measured at forward viewing bands (3-5) and the backward viewing bands (8-10) are used for cloud discrimination. The cloud detection algorithm (Ishida et al. 2009, 2018) uses reflectance (at the top of atmosphere) of these bands for detecting clouds from 11 recurrences (one month before and after the observation date) (GOSAT-2 TANSO-CAI-2 L2 Cloud Discrimination Processing ATBD). A flow-chart of the Cloud and Aerosol Unbiased Decision Intellectual Algorithm (CLAUDIA3; Ishida et al., 2018; Oishi et al., 2017) employed for cloud-screening of GOSAT-2 CAI-2 data is given in Supplementary Figure-S2. CLOUDIA3 is designed to automatically find the optimized boundary between clear and cloudy areas based on a supervised pattern recognition which uses support vector machines (SVM; Oishi et al., 2017). Before using the radiance (L1B) data in CLAUDIA3, a pre-processing is done to discriminate day and night, saturation flag, missing flag, polar region, water and land areas and sun-glint area for water area except the Polar Regions. Following this, solar reflection properties by clouds and ground surface are examined, which includes: (i) solar reflectance and reflectance ratio in the VIS and SWIR regions, (ii) wavelength dependence of reflectance in the VIS and NIR region, (iii) NDVI test for cloud discrimination over vegetated areas, and (iv) reflectance ratio between NIR and SWIR bands for cloud discrimination over desert areas (details in Cloud Discrimination Processing ATBD). Subsequently, this information is used in the CLOUDIA3 algorithm, which performs the cloud discrimination by SVM (Ishida et al., 2018) in order to objectively determine thresholds using multivariate analysis. SVM is one of the supervised pattern recognition methods, which first determines a decision function (called separating hyperplane) that defines clear or cloudy conditions according to the features of training samples (support vectors) in combination with a decision function.

The next step after cloud discrimination is the detection of cloud shadows. A minimum reflectance criterion is used for this purpose (Fukuda et al., 2013), which incorporates the difference between first and second minimum reflectance at UV (339 nm in forward viewing band-1 and 377 nm in backward viewing band-6), visible (670 nm in forward viewing bands-3 and backward viewing band-8) and NIR (865 nm in forward viewing band-4 and backward viewing band-9) bands. The first and second minimum reflectance at 670 nm are selected from multiple day from about two-months data between $X_{day} - n1$ and $X_{day} + n2$ day, where X_{day} is an analysis day and n1 and n2 are the number of scenes required before and after the analysis date that take the same path as the analysis date. When the difference between first and second minimum is smaller than a threshold for band-1 (339 nm; forward viewing) and band-6 (377 nm; backward viewing), i.e., $R_{(2nd,min)band1,6}$ - $R_{(1st,min)band1,6}$ < 0.10; and greater than a threshold for band-4 (865 nm; forward viewing) and band-9 (865 nm; backward viewing), i.e., $R_{(2nd,min)band4,9}$ - $R_{(1st,min)band4,9}$ > 0.06; the first minimum reflectance of the bands 3 and 8 are judged to be affected by cloud shadows and the second minimum reflectance is selected as a minimum reflectance (Fukuda et al., 2013). The advantage of using near-UV wavelengths is that the surface reflectance at UV over land is smaller than that at visible wavelengths, as is

already applied for aerosol retrieval in TOMS and OMI (Torres et al., 1998; 2002; 2007; 2013) and the MODIS (Hsu et al., 2004; 2006).

After cloud and cloud shadow correction, the influence of atmospheric molecular scattering (Rayleigh scattering) is corrected from the minimum reflectance data. For this, radiative transfer calculations are performed in advance and look-up tables (LUT) are generated for atmospheric single- and multiple-scattering components of reflectance, unidirectional transmittance, and spherical albedo. Based on this, the effect of atmospheric molecular scattering is removed from the minimum reflectance data for different combinations of satellite-solar geometry. The surface albedo (A_g) is estimated from the atmospherically corrected minimum reflectance data using the following equations:

$$A_g = \frac{1}{C + r_{Band(i)}(\tau)} \tag{1}$$

$$C = \frac{t_{Band(i)}(\tau; \mu_o) t_{Band(i)}(\tau; \mu_1)}{R_{Band(i)}(\mu_1, \mu_o, \varphi)/T^2_{gas,Band(i)} - R_{Atmos(i)}(\mu_1, \mu_o, \varphi)} \tag{2}$$

Where μ_1, μ_o, ϕ are satellite zenith angle, solar zenith angle and relative azimuth angle respectively. R and T_{gas} denote apparent reflectance and transmission of light absorbing gas. The subscript "i" denotes observation band number from 1 to 10, $R_{atmos} = R_{single} + R_{multiple}$. τ is the optical thickness of the atmosphere, $t(\tau; \mu_o)$ and $t(\tau; \mu_1)$ are unidirectional transmittance, $r(\tau)$ is spherical albedo. t, r, and T_{gas} are obtained by LUTs (details in GOSAT-2 TANSO-CAI-2 L2 Pre-processing ATBD).

Retrieval of AOD and SSA

For the retrieval of columnar aerosol optical depth (AOD) and aerosol single scattering albedo (SSA) from the satellite received path radiances, a multiple-wavelength multiple-pixel (MWPM) inversion algorithm (Hashimoto and Nakajima, 2017) is used. This algorithm utilizes information contained in different pixels with different surface reflectance and it is assumed that aerosol properties vary slowly or almost negligibly in the horizontal direction (over different pixels) where the variations in surface properties are significant. Thus, the variations in the upward radiances over different pixels are assumed to be varying due to variations in surface reflectance at the respective pixels. Under this assumption, when there is an increasing aerosol load over all the pixels under consideration, the satellite reaching upward (backscattered) radiance increases over a dark surface. In compared to that, the change in the magnitude of upward radiance with increasing aerosols load over brighter surface reflectance is lower. Because, as the surface reflectance increases, the absorption of light in the atmosphere and the backscattering of radiance to the surface increase which results in decrease in net upward radiance. At some specific surface reflectance, the net upward radiance does not change with increasing aerosol load in the atmosphere, as the increasing absorption and backscattering of light due to aerosol load in the atmosphere fully compensates the increasing surface reflectance, resulting in net zero upward radiance. This kind of surface reflectance is termed as neutral reflectance where the apparent reflectance is equal to surface reflectance. Difference between apparent reflectance and surface reflectance is the net reflectance. For surface reflectance beyond the neutral reflectance, the surface reflectance dominates over the apparent reflectance, resulting in darkening effect of atmosphere on the surface (Kaufman et al., 1987). It is to be noted that the balance between the brightening of the surface by atmospheric scattering and darkening by aerosol absorption (i.e., critical surface reflectance or neutral reflectance) varies with the values of SSA. For each value of SSA, there is a corresponding value of neutral or critical reflectance, for which the upward radiance is almost independent of the AOD.

The above methodology adapted by Hashimoto and Nakajima (2017) is an extension of the method by Kaufman (1987), however using the information of aerosol and surface properties at multiple wavelength and multiple pixels of satellite

image. As the variation in radiances take place with variation in AOD depending on aerosol light scattering (or single scattering albedo - SSA) and surface reflectance, this principle is suitable for successful retrieval of SSA over different surface reflectance areas. Considering no change in the measured radiances between a clear (low AOD) and a hazy (high AOD) day, the critical reflectance is determined from satellite radiances. The spatially distributed critical surface reflectance is then used to derive AOD and SSA over multiple pixels by using a theoretical relation between critical reflectance, AOD and SSA, computed for a given aerosol scattering phase function. Radiative transfer equations (RTE) are solved together for information contained in radiances at each of the pixels with different surface reflectance (Hashimoto and Nakajima, 2017). The simultaneous use of short and long wavelengths in the CAI-2 bands is very effective for aerosol retrieval when the surface is covered by vegetation and bare soil depending on the location.

The inversion method developed based on the above concept (Hashimoto and Nakajima, 2017) is a combination of maximum a posteriori optimal method (Rodgers, 2000) and a special formulation of GRASP method (Dubovik et al., 2011; 2014). The inversion analysis is conducted over different sub-domains, where the retrieved values of the optimal set of AOD, SSA and surface reflectance at one domain are considered as Dirichlet boundary conditions for the next domain.

Uncertainty in AOD and SSA retrieval

The uncertainty in the retrieval of AOD using MWPM inversion algorithm over heterogeneous surfaces is found to be within ± 0.062, ± 0.048 and ± 0.077 for $AOD500_{fine}$, $AOD500_{coarse}$ and $AOD500_{total}$ respectively (Hashimoto and Nakajima, 2017). These results are based on the comparison of AOD retrieval from CAI measurements of radiances with AOD data obtained from AERONET (Holben et al., 1998) and SKYNET (Nakajima et al., 2007). Comparison of the CAI-retrieved SSA (at 674 nm) with that of the AERONET observed values (SSA at 675 nm) revealed the retrieval accuracy of SSA within 0.05. Over the homogeneous surface, the random measurements error of the retrieval parameters is below 2%.

Deriving BC mass concentration

The BC mass concentration (M_{BC}) is derived (Release Note: GOSAT-2 TANSO-CAI-2 L2 Aerosol Property Product, 2021) using the size distribution of fine mode particles, the fine mode AOD at 550 nm ($\tau 550_{fine}$), and the volume fraction of BC in fine mode particles (f_{BC}). The expression for M_{BC} can be given as

$$M_{BC} = \frac{1}{m} f_{BC} \rho_{BC} \int_{r_{min}}^{r_{max}} \frac{dV_{fine}(\tau 550_{fine})}{dlnr} dlnr \qquad (3)$$

Here, ρ_{BC} is density of BC (~ 1.8 g cm^{-3}), V_{fine} is the volume of fine mode particles, r is the radius of particles and m the aerosol height information parameter (~ 1000 m in this study). As M_{BC} is 1000 m averaged values of column fine mode aerosol particle amount in this study, thus the definition is different from BC mass concentrations obtained by in-situ ground-based measurements.

For the estimation f_{BC}, an internal mixture of fine-mode aerosols (composed of 75% sulfuric acid and soot; mode radius $\sim$ 0.175 µm and dispersion of the lognormal volume size distribution ~ 0.8) is considered and the volume fraction of soot particles (indicated as soot volume fraction, SF) is considered representative of aerosol light absorption by the fine-mode particles. Thus, $f_{BC} = V_{soot}/V_{fine}$, where V_{soot} is the soot volume in the fine mode only. In the beginning, a-priori value of soot is assumed as 0.01 and the retrieval parameter 'u' is investigated based on its' a-priori state 'u$_a$'. Several a-priori values around the true-states 'u$_t$' are considered in the experiment; such as $u_t \pm 1.0u_t$ for $AOT_{500fine}$, $AOT_{500coarse}$, and SF, and $u_t \pm 0.01u_t$ for surface reflectance. The a-priori values of $AOD_{500fine}$ and $AOD_{500coarse}$ are considered as 0.2. The iteration in the solution search is stopped when the threshold is < 0.02.

In this simple approximation, various other mixing states of aerosols such as half internal and half external, core shell, and aggregated ones (Hashimoto et al., 2017 and references therein) are ignored. Thus, SF should be regarded as an equivalent value of soot in the fine mode particles, where the absorption property of aerosol is attributed only to the BC particles in the fine mode regime. As the BC mass distribution shows a mode of 100 – 300 nm (Kompalli et al., 2021) having stronger absorption in the NIR region, the light absorption by BC is significant mostly in the fine mode regime. The light absorption by other light-absorbing aerosols such as brown carbon and dust (coarse particles) responds strongly to radiation perturbation in the near-UV region (Mahowald et al., 2013). For the wavelength dependence of light absorption by BC, the complex refractive index of soot particles (d'Almeida et al., 1991) is considered in the retrieval process. However, the aerosol light absorption in the coarse mode domain is not considered in this assumption.

With a view to understanding the uncertainty of satellite received radiances due to different mixing states of aerosols with varying BC fractions, a sensitivity study is carried out using 6S radiative transfer code (Vermote et al., 1997). 6S code is widely used for the simulation of satellite reaching radiation for different combinations of sun-satellite geometry under various conditions of aerosol load in the atmosphere. The surface is considered as homogeneous Lambertian surface in the simulations. It is observed (Supplementary Figure-S3) that the sensitivity of BC-fraction (at 880 nm) to satellite reaching radiation is significantly improved under higher aerosol loadings (AOD > 0.5) as well as under higher surface reflectance conditions, while there is no marginal distinction between BC and non-BC conditions for AOD < 0.5. The sensitivity study also clearly indicates that the satellite reaching radiation for 1% BC in the aerosol mixture are affected by as low as 5% for variation in dust fraction from 1% to 10% during low aerosol loading conditions (AOD ~ 0.1). For higher BC fraction (~ 10%) in the aerosol mixture under heavy aerosol loading conditions (AOD ~ 2.0), the variation in dust fraction from 1% to 10% is found to change the apparent reflectance by ~10% for surface conditions of higher reflectance (~ 0.5), while the variability is much larger (~ 15%) for low surface reflectance conditions (~ 0.1). This exercise clearly indicates that the uncertainty in satellite retrieval of BC arising out of ignoring the contribution of dust in the aerosol mixture is less over dark surfaces when the aerosol load is low. Similarly, the retrieval uncertainty is lower over brighter surface when the aerosol load is high. Overall, it is to be noted that consideration of the accurate mixing state (internal and external) of aerosols is important for accurate computation of effective refractive index and size distribution of aerosols. Lesins et al., (2002) have reported that the optical properties of the internal mixture of BC and ammonium sulfate can differ by as high as 25% (for the dry case) and 50% (for the wet case) from that of its external mixture.

Within the above-mentioned uncertainties, the sensitivity study has shown that SF is underestimated under low aerosol loading conditions (AOD < 0.2) over highly-reflective surface. This is because the retrieval uncertainty of AOD is higher over the high-reflectance surface which leads to the overestimation of $AOD_{500fine}$. For higher aerosol loading condition ($AOT_{500total}$ > 0.4), the MWPM algorithm simultaneously determines AOT500fine, AOT500coarse, and SF within error of ±0.06, ±0.05, and ±0.05 respectively.

2.2 Estimation of BC Column Optical Depth

Employing the values of soot volume fraction (f_{BC}) as well as mass absorption efficiency of BC with its columnar content, the columnar optical depth due to BC (BC_{AOD}) over the study domain is estimated. Following *Wang et al.*, (2013), the expression for optical depth due to BC (BC_{AOD}) can be given as

$$AOD_{BC} = \sigma_{abs}\rho_{BC}V_{BC} \qquad (4)$$

where, σ_{abs} is the mass absorption coefficient due to BC, ρ_{BC} is the density of BC (assumed as 1.8 g cm^{-3}), $V_{BC}(= f_{BC}.V_{total})$ is the volume concentrations of BC in the vertical column and V_{total} is total volume concentrations of aerosols in the vertical

column. Following Schuster et al., (2005), the volume concentrations of BC can be estimated from the columnar mass concentrations of BC_{col} (in µg m^{-2}, up to 1 km altitude in the present study) as:

$$BC_{col} = f_{BC}\rho_{BC} \int \frac{dV}{dlnr} dlnr \tag{5}$$

For estimating σ_{abs} for the columnar content of BC, a constant value of mass absorption efficiency, MAE = 10 m^2 g^{-1} is assumed (Kondo et al., 2009). BC mass absorption efficiency (i.e., absorption coefficients of the particles divided by the mass concnetrations of BC in the aerosol) indicates the light absorbing efficiency of certain amount of BC having different mixing and sizes (Martins et al., 1998). Several investigators have reported the MAE of BC varying between 4.3 to 15 m^{2}g^{-1}, even though the measured values for freshly generated BC fall within a relatively narrow range of 7.5 ± 1.2 m^{2}g^{-1} at 550 nm (Bond et al., 2013). Sand et al., (2021) have also reported a model mean value of MAC as 10.1 (3.1 to 17.7) m^2 g^{-1} (550 nm).

2.3 Surface BC Measurements in the ARFINET

Near surface mass concentrations of BC are obtained from the multi-wavelength aethalometer measurements in the ARFINET. The aethalometers measure the rate of increase in optical absorption due to BC deposit on a filter spot (Hansen et al., 1984). By knowing the change in the optical attenuation by the volume of air (i.e., the mass flow rate multiplied by the sampling time) and the spot area of the filter, the BC concentrations (in µg m^{-3}) can be estimated. The measurement of the rate of change of optical absorption on a single collecting spot can be subject to non-linearity due to the nature and composition of the aerosol (Park et al. 2010), which is prominent in earlier-model Aethalometers (models AE-16, AE-21, AE-22, AE-31, AE-42-2 and AE-42-7) as against the latest model (AE-33). As the spot gradually becomes darker, the calculated output concentration can be under-reported; reverting to the correct value when the tape advances to a fresh spot. Provided that a continuous data record exists, which spans several tape advances due to loaded and fresh tape spots, it is possible to post-process the data. This recalculates the BC data for each wavelength, in addition to providing the value of the filter loading compensation parameter, which is found to be indicative of aerosol properties (Drinovec et al., 2017). In this study, the quality of BC data is ensured following the uniformity of measurements by aethalometers of different models. Regular servicing, calibrations and inter-comparison of the instruments are also made in the ARFINET for quality data collection. The overall uncertainty in BC mass measured by the aethalometer is estimated at about 10% and more details are available in Gogoi et al., (2017).

2.4 Fire Radiative Power

To understand the spatio-temporal distribution of BC with reference to the occurrences of biomass burning events across the globe, MODIS Collection 6 Active Fire Products (MCD14ML), viz., fire radiative power (FRP) and fire types are used in this study. MCD14ML (global fire location products) contains the geographic coordinates of individual fire pixels from both Terra and Aqua satellites. The FRP or fire radiative energy (FRE) is the emitted radiant energy released during biomass combustion episodes, which is a suitable parameter to determine the biomass combustion rates and the rate of production of atmospheric pollutants. The detailed principle behind the remote determination of FRP products used in this study is available in Wooster et al., (2003). This technique, called MIR radiance method, uses data from MIR spectral channel to estimate FRP. The principle behind this technique is that the ratio of the total power emitted over the entire MIR wavelength range to the power emitted at 4 µm is approximately constant within a temperature range (~ 600 – 1500 K) appropriate to most wildfires. Following this, the MIR radiance '$L_{MIR,h}$' of a fire hotspot pixel containing 'n' sub-pixel thermal components is expressed as

$$L_{MIR,h} = a\varepsilon_{MIR} \sum_{i=1}^{n} A_n T_n^4 \tag{6}$$

Here, ε_{MIR} is surface spectral emissivity in the appropriate MIR spectral band, A_n = fractional area of nth surface thermal component within the individual ground pixel, and T_n = temperature of nth thermal component (K). The constant 'a (W m^{-4} sr^{-1} µm^{-1})' is determined from empirical best fits relationship between blackbody temperature and emitted spectral radiance at single wavelength. The above equation when combined to the spectral radiance $L(\lambda)$ emitted by a blackbody at wavelength λ, it relates FRP to the MIR spectral radiance of the hot pixel. Thus,

$$FRP_{MIR} = \frac{A_{sampl}\sigma\varepsilon}{a\varepsilon_{MIR}}L_{MIR,h} \qquad (7)$$

Where, A_{sampl} is ground sampling area (m^2), σ is Stefan-Boltzmann constant. With A_{sampl} = 1.0 x 10^6 m^2, the FRP for MODIS pixels are derived as

$$FRP_{MIR} = 1.89 \text{ x } 10^7(L_{MIR} - L_{MIR,bg}) \qquad (8)$$

Here, $L_{MIR,bg}$ is background MIR radiance estimated from neighbouring non-fire ambient pixels. All radiances are in units of Wm^{-2} sr^{-1} µm^{-1} and *FRP* in units of Js^{-1} of Watts.

3 Results and Discussions

3.1 Regional distribution of BC over India

GOSAT-2 makes 89 laps for observing the whole globe in 6 days (swath ~ 920 km). Starting from the ascending node, each satellite revolution data is defined as a CAI-2 scene. Each of the scenes is divided in to 36 equal parts (each part is called as frame) by the argument of latitude at observation point of central pixel. A file unit of CAI-2 archives the data of one frame. Since the scene for CAI-2 archives the data of only day side, 18 files are generated from one satellite revolution. In the present study, data from individual files are analyzed to estimate daily as well as monthly average values. For the distinct geographical regions of India with a variety of emissions and transformation processes of carbonaceous aerosols, the spatiotemporal distributions of BC from satellite (GOSAT-2 CAI-2) retrieval (of the years 2019 and 2020) and surface measurements (climatological data) in the ARFINET are shown in Fig. 2 (December-January-February, DJF), Fig. 3 (March-April-May, MAM) and Fig. 4 (June-July-August, JJA), representing three distinct periods of winter, pre-monsoon, and monsoon, respectively.

In winter (DJF), the surface observations (Fig. 2) depict the highest BC mass concentrations (M_{BC}) in the IGP (~ 13.67 ± 5.65 µg m^{-3}) followed by NEI (~ 12.35 ± 4.87 µg m^{-3}), with M_{BC} exceeding 7 µg m^{-3} in most locations. Several polluted locations exhibit values above 15 µg m^{-3}, with the highest values occurring in urban centers. BC concentrations remain lower (< 5.5 µg m^{-3}) over the NWI (~ 4.67 ± 3.48 µg m^{-3}), CI (~ 5.36 ± 0.80 µg m^{-3}) and PI (~ 4.51 ± 3.02 µg m^{-3}) and lowest across the HIM (including sub-Himalayan and foothill sites; average BC ~ 2.26 ± 1.75 µg m^{-3}). Like the surface observations, satellite retrievals also show higher values of BC over the IGP and NEI with magnitude comparable to those of the surface BC measurements. Pockets of higher BC are also apparent at some of the locations of PI from both satellite retrievals and surface measurements. It is also consistent with the surface observations that satellite retrieved BC is higher over the eastern coast of India. However, it is to be noted that the intra-seasonal variability in the case of satellite retrieval is very significant while considering the regional distribution of BC. On the other hand, near surface measurements of BC at the point locations of the ARFINET show nearly consistent values at different months of winter.

In pre-monsoon (MAM, Fig. 3), the surface measurements show gradual decline in BC from that of the DJF, with 50-60% declining of seasonal average surface BC concentrations at the hotspots of IGP (~7.05 ± 1.78 µg m^{-3}) and NEI (~ 4.88 ± 1.13

μg m^{-3}). The intra-seasonal variability of BC at different point locations of the ARFINET is also apparent during this period with values of BC decreasing from March to May. In line with this, the satellite retrievals also clearly show gradual decline in BC from DJF to MAM, retaining the consistent features of the regional hotspots of BC over the IGP and NEI as seen in the surface measurements. The intra-seasonal variability in the satellite retrieval is also nearly similar to that of the surface observations. Moreover, both in satellite retrievals and surface measurements, BC remains below 3 μg m^{-3} over the NWI, CI and PI regions.

In monsoon (JJA, Fig. 4), the surface BC concentrations significantly reduce at most of the locations of ARFINET. The average values of surface measured BC over the IGP and NEI are 3.93 ± 1.64 μg m^{-3} and 2.64 ± 1.30 μg m^{-3} respectively, with M_{BC} < 2 μg m^{-3} over the rests of the regions. Resembling this, the satellite retrievals also show decline in BC from MAM to JJA over the IGP and NEI. However, as opposed to the surface measurements, satellite retrievals show higher BC (> 3 μg m^{-3}) in several pockets of CI and PI regions, particularly during July and August with values higher than during MAM.

Based on the above observations it appears that the spatio-temporal distribution of BC as obtained from satellite retrievals show better consistency with the surface measured BC over the Indian region during DJF and MAM. As the rise in temperature caused by increased solar heating during MAM and JJA results in strong thermal convection over the Indian region (especially in the northern part), this leads to dilutions of near-surface aerosol concentrations. Depending upon the geographic position and local meteorological conditions, the strength of convection varies from one location to the other. As the satellite retrieve BC is 1-km column average BC concentrations, the variation in the vertical distribution of BC may lead to variable associations between satellite-retrieved and surface measured BC concentrations at distinct geographic locations of India. More details on these aspects are discussed in the following sections. Apart from the vertical heterogeneity, the various other factors that may lead to discrepancy in the satellite retrieval of BC include the bias caused by the cloud-screening algorithm, especially during JJA when the cloud cover over the Indian region is extensive. Moreover, CLAUDIA3 is unable to detect optically thin clouds. Lack of accurate detection of cloud shadow can also cause overestimation in the retrieve values of aerosol parameters from CAI-2 measurements. Since the revisiting time of CAI-2 is long (6 days), the minimum reflection criterion based on the consideration of 2 months data (one month prior and after the measurement days) can lead to large uncertainty in cloud-shadow detection, hence the accurate estimation of minimum surface reflectance. Subsequently, these errors can propagate and add uncertainty in the accurate estimation of aerosol parameters from CAI-2 measurements.

Satellite retrievals vs climatological surface BC concentrations

The comparison of the 1 x 1 degree area average BC (around each of the observational sites) from satellite retrievals with the climatological (2015-2019) monthly average surface BC concentrations (obtained during 13:00 to 14:00 hrs. local time) at different months of winter, pre-monsoon and monsoon show the consistency of satellite retrievals (Supplementary Fig. S4; the statistical fit parameters are given in Supplementary Table T2). It is evident that the linear correlation between the two data sets is highest in May (R ~ 0.79). R > 0.6 during February through August. In the months of December and January, R < 0.5. On a seasonal term (Supplementary Fig. S5), the satellite retrievals and surface observations show better agreement during MAM (R ~ 0.70). In JJA, the correlation between the two data sets is weak (R ~ 0.50) and the least in DJF (R ~ 0.43). This indicates that even though satellite retrievals and surface observations show good agreement at the regional hotspots of BC over India during winter and pre-monsoon months, there is a lack of consistency between the two datasets in winter at some of the other ARFINET observational sites.

The discrepancies between satellite retrievals and ground-based observations can be attributed to the varying role of geographical features, as well as the heterogeneity of BC abundance and vertical their distribution in the atmosphere during different seasons. As the satellite retrieved BC is 1-km column average fine mode particle concentrations, the role of planetary boundary layer (PBL) dynamics and columnar pattern of BC distribution are crucial in understanding the association between satellite and surface measured BC. In locations having PBL height of ~ 1 km is expected to demonstrate better associations between the two than in locations with much extended (> 1 km) or shallow (< 1 km) PBL. Thus, the spatio-temporal variability of PBL could be an important factor in explaining the association between satellite retrieval and climatological surface BC measurements.

The regional average BC over the entire Indian region (Fig. 5) shows that the satellite-retrieved BC differ from surface-measured BC by < 33% in most months, except July and August (> 50%). In February-August, the magnitudes of satellite retrieved BC are lower (underestimates, as much as 32.6% in February) compared to surface measurements; while it is opposite (overestimates) in December-January and June-August, with highest overestimation in August (~ 69%). Seasonally, the difference between the two data sets over the entire Indian region is < 20% in DJF and MAM and ~ 53.5% in JJA (Table-1). In general, the surface measurements of BC concentrations over the entire Indian region show a gradual decline from its highest values in DJF (2.54 ± 0.11 μg m^{-3}) through MAM (2.06 ± 0.47) to its lowest value in JJA (1.11 ± 0.17 μg m^{-3}). Similar to this, the 1-km column average satellite retrieved BC also show highest BC concentrations over the collocated locations of India during DJF and their gradual decline in MAM. However, the satellite retrieved BC are found to be higher in JJA than in MAM, as opposed to the pattern seen in the case of surface measured BC. These observations hint again the discrepancy between satellite retrievals and surface measured BC in JJA, while their absolute magnitudes and regional distributions are nearly consistent during DJF and MAM in most locations.

Satellite retrievals vs. daily surface BC concentrations

After studying the regional distribution and the association between satellite-retrieved BC and climatological monthly average surface BC levels in DJF, MAM and JJA, we examine simultaneous day-to-day values of BC from the satellite retrievals and surface measurements. Since the satellite retrieved BC corresponds to 1-km column average fine mode particle concentrations, the measured BC concentrations in the surface are normalized to a PBL height of 1 km for utilizing in the validation experiment. For this, it is assumed that BC possesses uniform vertical profile within the well mixed PBL and their concentrations are negligible above the PBL. Thus, the expression relating the 1-km column concentration of BC in the surface ($BC_{\text{SUR-N}}$) and the actual BC concentrations measured at the surface within the PBL (BC_{SUR}) can be given as

$$BC_{\text{SUR-N}} = BC_{\text{SUR}} / h \qquad\qquad (6)$$

Here, h is the height of the PBL layer, and the measured concentrations of BC in the PBL is assumed as the sum of concentrations in each layer of thickness 'dh' from surface to the PBL height h (i.e., $BC_{SUR-N} = \int_0^h BC_i(h)dh$; here, '$i$' is the number of layers from 0 to h). For $h = 1$, $BC_{\text{SUR-N}} = BC_{SUR}$. The higher the PBL height above 1 km, the greater the measured BC concentration in the surface than that measured within 1 km PBL and vice versa. As the seasonally varying PBL heights at different ARFINET sites might play an important role in understanding the association between the satellite retrieval and the surface measured BC, the normalized values of surface BC concentrations (BC$_{\text{SUR-N}}$) are used in this section to evaluate and validate the simultaneous (corresponding to satellite overpass time) day-to-day values of satellite retrieved (1-km column average) BC. The PBL height information is obtained from ERA5 (Hersbach et al., 2020). Similar methodology has been reported by Bao et al., (2019).

The frequency distributions of the absolute differences between the two datasets are shown in Fig. 6a, which indicate good agreements between the simultaneous satellite retrieved BC (BC$_{\text{SAT}}$) and normalized surface measured BC (BC$_{\text{SUR-N}}$)

concentrations. Approximately 60% of the BC_{SAT} is comparable (absolute difference < 2 µg m^{-3}) to BC_{SUR-N} during all periods of DJF, MAM and JJA. As shown in Fig. 6b, the correlation between the two data sets having absolute difference < 2 µg m^{-3} is highest in MAM (R ~ 0.76), followed by DJF (R ~ 0.73) and JJA (R ~ 0.61).

The absolute differences between the two data sets are relatively smaller (Fig. 7) at the PI locations where BC concentrations and seasonal variability are also lower than the northern Indian locations (seasonal mean values of surface measured BC at each of locations are shown by the histograms). It is further evident from Fig. 7 that the absolute difference between BC_{SAT} and BC_{SUR-N} reduce significantly from that between BC_{SAT} amd BC_{SUR} at several locations of PI and northern India, especially during the MAM and JJA. During winter, even though the abundance of BC is confined near to the surface due to shallow PBL condition, the noon time PBL is much extended (close to or beyond 1-km) over most of the Indian locations (the spatio-temporal variability in PBL height is shown in supplementary Fig. S6). Thus, BC_{SUR-N} follows the same general trend as the BC_{SUR}, indicating that noon-time surface measured BC concentrations during winter are similar to the 1-km column average BC. During MAM, the locations with PBL heights extended above 1-km are found to show good association of BC_{SAT} with BC_{SUR-N} than that of BC_{SAT} with BC_{SUR}. In JJA, the height of PBL is found to be highly region specific. At some of the locations, the PBL is much above 1-km (e.g., CHN and KDP), while some other locations show the opposite pattern (i.e., TVM, PBL height below 1 km). The locations with PBL heights below 1-km are found to show lower absolute difference between BC_{SAT} and BC_{SUR-N} than that between BC_{SAT} and BC_{SUR}. However, it is also to be noted that the simultaneous data of satellite-retrieved and surface measured BC are less in JJA as compared to DJF and MAM. Overall, it is observed that, in most of the locations, the absolute difference between BC_{SAT} and BC_{SUR-N} is lower than that between BC_{SAT} and BC_{SUR}. This leads to better correlation between BC_{SAT} and BC_{SUR-N}, especially during JJA where the correlation between BC_{SAT} and BC_{SUR-N} is much better (R ~ 0.61) than that between BC_{SAT} and BC_{SUR} (R ~ 0.38).

The northern part of India experiences significant seasonal changes in terms of incoming ground reaching solar radiation, with intense radiation during the pre-monsoon and monsoon months (Soni et al., 2012; Subba et al., 2022). This leads to significant seasonality in the PBL, that controls the vertical dispersion and hence the near surface loading (reduction) of aerosols. Based on air-borne in-situ measurements, Nair et al., (2016) have shown large seasonality (variation from winter to pre-monsoon) in the vertical profile of aerosol absorption coefficients over the IGP and Western India. Similarly, Brooks *et al*., (2019) have reported nearly uniform distribution of BC through the vertical profile over NW India, IGP and the outflow region of IGP during monsoon.

Apart from seasonality, BC over the continental locations with low altitude above mean sea level shows significant diurnal variability with day time low and night time high with a sharp peak after the sunrise. The increased convective activity during day time leads to deeper and more turbulent boundary layer and a faster dispersion of aerosols resulting in a decrease in concentration near the surface. Several recent studies have reported the prominent effect of PBL on the diurnal variability of BC, the amplitude of which vary significantly across the country, especially during winter (Babu et al., 2002; Beegum et al., 2009; Pathak et al., 2010; Gogoi et al., 2013, 2014; Kompalli et al., 2014; Prasad et al., 2018 etc.). In addition to the variability in atmospheric mixing and vertical dispersion of BC, accurate estimation of surface properties is another important parameter in the satellite retrieval. Better estimates of surface properties during DJF and MAM could be the reason for improved correlations between satellite retrievals and surface BC concentrations, while the adverse atmospheric (clear, hazy or cloudy) and land surface (wetter soils) conditions might affect the ability to estimate fine mode aerosol concentrations during JJA.

The uncertainty of switching columnar concentration to near ground

With a view to understanding the uncertainty arising out of the consideration of uniform distribution of BC within the PBL, the vertical profiles of BC obtained during two distinct periods of winter (December) and spring (May) over two distinct

geographic locations (Hyderabad – HYD and Lucknow - LKN) of central and northern India are considered based on data collected on-board an instrumented aircraft as part of Regional Aerosol Warming Experiment - RAWEX (Babu et al., 2016; Gogoi et al., 2019). As the vertical distribution of BC is not uniform in the real scenario, the uncertainty arises in the estimated column BC amount from surface BC measurements as well as in the derivation of BC from satellite based measurements, which also assumes uniform vertical distribution of BC within the well mixed boundary layer. The supplementary Fig-S7 clearly shows that the vertical profiles of BC possess significant seasonality, in addition to their spatial variability. Up to the ceiling height of 1 km, it appears that the average BC concentrations within this column vary as high as 28% (HYD) to 58% (LKN) from that of the surface BC concentrations in winter. Compared to this, columnar variability in spring is relatively less (32%) at LKN. On the other hand, columnar distribution of BC at HYD continued to show a sharp reduction with height till 1 km altitude, but with subsequent enhancement in BC concentrations at higher heights. Based on Model for Ozone and Related chemical Tracers, version 4 (MOZART-4) simulation studies, Bao et al., (2019) have also reported that BC above the PBL contributes by 5%-80% to the column concentrations, even though the distribution of BC within the PBL is nearly uniform."

3.2 Soot Volume Fraction, SSA and BC Column Optical Depth

The soot volume fraction (*SVF*) or the volume fraction of BC in fine mode particles is an important parameter to understand the relative dominance of soot in the fine mode aerosol load in the column. Accurate estimate of SVF is essential for the quantification of the radiative effects of BC (Wang et al., 2016). In this study, an internal mixture of fine-mode aerosols is adapted to represent aerosol light absorption by SVF in the fine-mode particles. The spatial distribution of the SVF at different months of winter, pre-monsoon, monsoon seasons (as shown in the supplementary Fig. S8) indicates that the ratio of soot in the entire aerosol mixture is as high as 5% over the IGP and northeastern parts of India. These values are similar to the mass fractions of BC reported by Gogoi et al., (2020) over the western, central and eastern part of the IGP based on air-borne in-situ measurements. The prior in-situ observation thus suggests that the values of SVF estimated from the satellite-based observation can capture the broad regional features of columnar amounts of soot in fine mode particle concentrations. Based on sensitivity studies, Hashimoto and Nakajima (2017) have reported that the detection of an absorption by soot and dust particles is less uncertain over a high-reflecting surface and is spectrally more sensitive to the measurements of radiation at 380 nm of CAI-2 bands.

The monthly mean regional maps of SSA (at 546 nm) are shown in the Supplementary Fig. S9. The figure shows very large spatio-temporal variability, with values of SSA < 0.92 over most parts of the Indian region in December and January. In December, pockets of lower SSA (as low as 0.8) are observed over the western IGP, the Himalayan foothills, the NEI, and central India. The values of SSA over the IGP remains low until March and April, which also depict low values (~ 0.8) in its western part. It is evident from these observations that satellite-based retrieval of SSA from CAI-2 observations is capable of quantifying the spatio-temporal distribution of SSA, as found in several in-situ measurements. Using aircraft measurements, Babu et al., (2016) have reported the values of SSA between 0.86 and 0.94 over different West Indian and IGP locations during the pre-monsoon (April-May) period. The values of SSA in our study are also in close agreement with those reported by Babu et al., (2016). In another study by Vaishya et al., (2018), it is reported that the values of SSA reduce significantly over the Himalayan foothills, the IGP regions and central India in pre-monsoon as compared to the winter season; while the peninsular India and adjoining oceanic regions show an increase. Just prior to the onset of monsoon, Vaishya et al., (2018) have also reported a decreasing gradient in SSA from the west to the east of IGP (~ 0.84 at west IGP, 0.73 at central IGP and 0.79 at eastern IGP; all at 530 nm). Over the oceanic regions, the values of SSA are generally high (> 0.95) and comparable to the surface values reported over the entire BoB (~ 0.93 during March-April) by Nair et al., (2008); Arabian sea (~ 0.9 in March) by Jayaraman et al., (2001).

In contrast to the above, the spatial distribution of SSA in our study is found to be different from that of the SSA derived from Ozone Monitoring Instrument (OMI) onboard Aura satellite. The monthly maps of the regional distribution of SSA (at 550 nm) from OMI (Level-3 daily 1 deg Lat/Lon global gridded product OMAERUVd; https://disc.gsfc.nasa.gov/datasets/OMAERUV_003/summary) are shown in Supplementary Fig. S10. The difference between the regional distribution of SSA from CAI-2 and OMI is higher during DJF, as compared to that during the other months. During DJF, CAI-2 retrievals show lower values of SSA over the Indian mainland as compared to the OMEAUVd SSA. During JJA, the spatial patterns of SSA are similar in both CAI-2 and OMEAUVd retrievals.

Similar to SVF and SSA, significant regional and seasonal differencesin BC column optical depths (BC$_{AOD}$) are seen (Fig. 8) with values ranging from as low as 0.001 to as high as 0.1. During pre-monsoon months, BC$_{AOD}$ over the IGP shows a gradual decline from March to May while the pattern is opposite over the NEI. BC$_{AOD}$ shows pockets of high values over NEI in May. Increase in total columnar AOD over the IGP from March to May (peaks in June) is also reported by earlier investigators (Gautam et al., 2009; 2010) as against the opposite trend (peak in March) over the NEI (Pathak et al., 2016). The higher BC$_{AOD}$ seen during December-April is indicative of the large amount of BC in the PBL during winter, both over the IGP (Singh et al., 2014; Vaishya et al., 2017) and NEI (Pathak et al., 2010; Guha et al., 2015) and its redistribution in the vertical column in the spring. This is further modulated by the occurance of seasonal fires over the Southeast Asia, which start appearing in December and increase in spatial extent and magnitude over time, to reach a peak during March to May (Sahu et al., 2021).

3.3 Global distribution of BC from satellite retrievals

Considering fair association between the satellite retrieved and surface observations of BC over the Indian region, the global distribution is BC is examined at different months of winter, pre-monsoon and monsoon (Figs. 9, 10 and 11, respectively). Along with this, the global distribution of Fire Radiative Power (FRP in MW; shown in Supplementary Figures S11, S12 and S13) and the type of fire (presumed vegetation fire, active volcano, static land shore and offshore; shown in Supplementary Figures S14, S15 and S16) are also examined. In the present study, day-time FRP with confidence level above 80% (high confidence; Giglio et al., 2020) is only used.

It is observed that the typical hot spots of BC prevailing throughout the year, though varying in magnitude, includes the biomass burning regions of South America, Africa, India and China. Enhanced values of BC are also seen in western Canada and USA, as well as over the Europe, Russia and part of China due to large fires occurring mainly in summer (JJA is marked by a large-scale outbreak of forest fires in the Russian Boreal Forests and South Africa; Justice et al., 1996; Wooster, 2004). The rainforest in Central Africa, being the largest biomass-burning region, shows large increase in the magnitude of BC during MAM and JJA. Amazon forest has lowest BC during MAM. These observations clearly indicate that the spatio-temporal variability of BC across the globe is mostly coincident with the regions of intense biomass burning activities, while BC over some regions of south Asia and China do not collocate with the biomass burning regions. Interestingly, some oceanic regions near the coast of western Africa also show higher values of BC during DJF and JJA. Some offshore fires are also seen to be contributing to the BC load in the west coast of Africa. In line with our observations, Barkley et al., (2019) have reported the transport of African biomass burning aerosols to oceanic regions in the southern hemisphere. In another study based on GEOS-Chem-TOMAS global aerosol microphysics model simulations, Ramnarine et al., (2018) have reported the abundance of organic aerosols and BC in the remote areas of southern hemisphere downwind of biomass burning emissions from the Amazon in South America, the Congo in Africa, and some regions of the boreal forests in North America and Siberia.

The satellite-based observation of global BC distribution in the present study is also found to be in line with those reported by Bond et al., (2004), showing the major areas of BC emissions over north, central and South America, Europe, Russia, Middle East, Pacific, Africa, China and India. As reported in their study, significant BC emissions from forest fire activity over South America and Africa is clearly detected by the satellite-retrieved BC in our study, which peaks during DJF and JJA. Similarly, significant BC load seen over the regions of Russia during May-June period is coincident with the open burning areas, as reported by Bond et al., (2004). Several studies (Dixon et al., 1993; Leskinen et al 2020 and the references therein) have reported that boreal forests and wild fires of Russia is crucial in the context of global carbon cycle, where large areas of Russian forest burn contribute to the net flux of carbon to the atmosphere.

4 Summary and Conclusions

This study investigates the regional and global distribution of BC based on satellite retrievals. Extensive measurements of near surface BC mass concentrations across a network of aerosol observatories (ARFINET) over the Indian region are used to evaluate the spatio-temporal distribution of BC retrieved from Cloud and Aerosol Imager - 2 on-board Greenhouse gases Observing Satellite – 2.

Regional distribution of BC from satellite retrieval (GOSAT-2 CAI-2) and surface measurements (ARFINET) during three distinct periods of December, January, and February (DJF); March, April and May (MAM) and June, July and August (JJA) showed good agreement between the two data sets over the Indian region. Especially during winter and pre-monsoon months, the satellite retrieval clearly identifies the regional hotspots of BC over India. The inter-comparison of satellite retrieved BC with the surface measurements revealed that the absolute difference between the two data sets is $< 2 \ \mu g \ m^{-3}$ over 60% of the observations in this study. Associations between the two data sets having absolute difference $< 2 \ \mu g \ m^{-3}$ is highest in MAM (R ~ 0.76), followed by DJF (R ~ 0.73) and JJA (R ~ 0.61).

The spatial distribution of the soot volume fraction (SVF) at different months of winter, pre-monsoon, monsoon seasons is similar to that of the spatial distribution of BC over the Indian region with the ratio of soot in the entire aerosol mixture is > 5% over the IGP and northeastern parts of India. Regional distribution of aerosol single scattering albedo (SSA) shows values as low as 0.8 over the IGP and the northwestern part of India during winter and pre-monsoon season. Similar to SVF and SSA, significant regional and seasonal differences in BC column optical depths (BC_{AOD}) are seen with values ranging from as low as 0.001 to as high as 0.1. These observations are consistent with the data reported from in-situ measurements or other remote sensing platforms. All of these observations thus suggest the applicability of the CAI-2 aerosol products.

Most of the spatio-temporal variability of BC across the globe occurs with intensive biomass burning activities, except for some regions of south Asia and China. Enhanced values of BC are also seen in western Canada and USA, as well as over the Europe, Russia and part of China due to large fires occurring mainly in summer. Across South America, Africa, India, and China, BC is generally higher throughout the year, not just during the biomass burning season.

Data availability

Details of ARFINET ground-based data used in this manuscript and the point of contact are available at http://spl.gov.in; "Research Themes"; "Aerosols and Radiative Forcing". Information about satellite (GOSAT-2 CAI-2) data is available at https://www.gosat-2.nies.go.jp/about/data_products/.

Authors Contributions

This study was conceived by MMG and SSB in collaboration with RI and MH. Data processing and statistical analysis of the
545 satellite and ground-based data were performed by MMG in consultation with SSB. All authors contributed to manuscript
conceptualization, editing and review for submission. MMG drafted the initial manuscript with input from SSB. As far as
ground-based aerosol data are concerned, MMG and SSB are responsible for BC data from the ARFINET; RI is the chief of
the science team of the GOSAT-2 project; and MH is the developer of the inversion code. All authors read and approved the
final manuscript.

550 **Competing interests**

The authors declare that they have no conflict of interest.

References

560 Babu, S. S. and Moorthy, K. K.: Aerosol black carbon over a tropical coastal station in India, Geophysical Research Letters,
29, 13-11-13-14, https://doi.org/10.1029/2002GL015662, 2002.

Babu, S. S., Manoj, M. R., Moorthy, K. K., Gogoi, M. M., Nair, V. S., Kompalli, S. K., Satheesh, S. K., Niranjan, K.,
Ramagopal, K., Bhuyan, P. K., and Singh, D.: Trends in aerosol optical depth over Indian region: Potential causes
and impact indicators, Journal of Geophysical Research: Atmospheres, 118, 11,794-711,806,
565 https://doi.org/10.1002/2013JD020507, 2013.

Babu, S. S., Nair, V. S., Gogoi, M. M. and Moorthy, K. K.: Seasonal variation of vertical distribution of aerosol single
scattering albedo over Indian sub-continent: RAWEX aircraft observations, Atmospheric Environment, 125, 312-323,
https://doi.org/10.1016/j.atmosenv.2015.09.041, 2016.

Bao, F., Cheng, T., Li, Y., Gu, X., Guo, H., Wu, Y., Wang, Y., and Gao, J.: Retrieval of black carbon aerosol surface
570 concentration using satellite remote sensing observations, Remote Sensing of Environment, 226, 93-108,
https://doi.org/10.1016/j.rse.2019.03.036, 2019.

Barkley, A. E., Prospero, J. M., Mahowald, N., Hamilton, D. S., Popendorf, K. J., Oehlert, A. M., Pourmand, A., Gatineau,
A., Panechou-Pulcherie, K., Blackwelder, P., and Gaston, C. J.: African biomass burning is a substantial source of
phosphorus deposition to the Amazon, Tropical Atlantic Ocean, and Southern Ocean, Proceedings of the National
575 Academy of Sciences, 116, 16216-16221, https://doi.org/10.1073/pnas.1906091116, 2019.

Beegum, S. N., Moorthy, K. K., Babu, S. S., Satheesh, S. K., Vinoj, V., Badarinath, K. V. S., Safai, P. D., Devara, P. C. S., Sacchidanand, S., Vinod, Dumka, U. C., and Pant, P.: Spatial distribution of aerosol black carbon over India during pre-monsoon season, Atmospheric Environment, 43, 1071-1078, https://doi.org/10.1016/j.atmosenv.2008.11.042, 2009.

580 Bond, T. C., Doherty, S. J., Fahey, D. W., Forster, P. M., Berntsen, T., DeAngelo, B. J., Flanner, M. G., Ghan, S., Kärcher, B., Koch, D., Kinne, S., Kondo, Y., Quinn, P. K., Sarofim, M. C., Schultz, M. G., Schulz, M., Venkataraman, C., Zhang, H., Zhang, S., Bellouin, N., Guttikunda, S. K., Hopke, P. K., Jacobson, M. Z., Kaiser, J. W., Klimont, Z., Lohmann, U., Schwarz, J. P., Shindell, D., Storelvmo, T., Warren, S. G., and Zender, C. S.: Bounding the role of black carbon in the climate system: A scientific assessment, Journal of Geophysical Research: Atmospheres, 118, 585 5380-5552, https://doi.org/10.1002/jgrd.50171, 2013.

Bond, T. C., Streets, D. G., Yarber, K. F., Nelson, S. M., Woo, J.-H., and Klimont, Z.: A technology-based global inventory of black and organic carbon emissions from combustion, Journal of Geophysical Research: Atmospheres, 109, https://doi.org/10.1029/2003JD003697, 2004.

Brooks, J., Allan, J. D., Williams, P. I., Liu, D., Fox, C., Haywood, J., Langridge, J. M., Highwood, E. J., Kompalli, S. K., 590 O'Sullivan, D., Babu, S. S., Satheesh, S. K., Turner, A. G., and Coe, H.: Vertical and horizontal distribution of submicron aerosol chemical composition and physical characteristics across northern India during pre-monsoon and monsoon seasons, Atmos. Chem. Phys., 19, 5615-5634, https://doi.org/10.5194/acp-19-5615-2019, 2019.

GOSAT-2 TANSO-CAI-2 L2 Pre-processing Algorithm Theoretical Basis Document, NIES-GOSAT2-ALG-20191008-008-01, 2020.

595 Choi, Y. and Ghim, Y. S.: Estimation of columnar concentrations of absorbing and scattering fine mode aerosol components using AERONET data, Journal of Geophysical Research: Atmospheres, 121, 13,628-613,640, https://doi.org/10.1002/2016JD025080, 2016.

d'Almeida, G. A., Koepke, P. and Shettle, E. P.: Atmospheric aerosols. Global climatology and radiative characteristics. A. Deepak Publishing, 1991.

600 Drinovec, L., Gregorič, A., Zotter, P., Wolf, R., Bruns, E. A., Prévôt, A. S. H., Petit, J. E., Favez, O., Sciare, J., Arnold, I. J., Chakrabarty, R. K., Moosmüller, H., Filep, A., and Močnik, G.: The filter-loading effect by ambient aerosols in filter absorption photometers depends on the coating of the sampled particles, Atmos. Meas. Tech., 10, https://doi.org/1043-1059, 10.5194/amt-10-1043-2017, 2017.

Dubovik, O., Herman, M., Holdak, A., Lapyonok, T., Tanré, D., Deuzé, J. L., Ducos, F., Sinyuk, A., and Lopatin, A.: 605 Statistically optimized inversion algorithm for enhanced retrieval of aerosol properties from spectral multi-angle polarimetric satellite observations, Atmos. Meas. Tech., 4, 975-1018, https://doi.org/10.5194/amt-4-975-2011, 2011.

Dubovik, O., Lapyonok, T., Litvinov, P., Herman, M., Fuertes, D., Ducos, F., Lopatin, A., Chaikovsky, A., Torres, B., Derimian, Y., Huang, X., Aspetsberger, M., and Federspiel, C.: GRASP: a versatile algorithm for characterizing the atmosphere, SPIE Newsroom, https://doi.org/10.1117/2.1201408.005558, 2014.

610 Dubovik, O., Lapyonok, T., Litvinov, P., Herman, M., Fuertes, D., Ducos, F., Lopatin, A., Chaikovsky, A., Torres, B., Derimian, Y., Huang, X., Aspetsberger, M., and Federspiel, C.: GRASP: a versatile algorithm for characterizing the atmosphere, SPIE Newsroom, https://doi.org/10.1117/2.1201408.005558, 2014.

Fukuda, S., Nakajima, T., Takenaka, H., Higurashi, A., Kikuchi, N., Nakajima, T. Y., and Ishida, H.: New approaches to removing cloud shadows and evaluating the 380 nm surface reflectance for improved aerosol optical thickness

615   retrievals from the GOSAT/TANSO-Cloud and Aerosol Imager, Journal of Geophysical Research: Atmospheres, 118, 13,520-513,531, https://doi.org/10.1002/2013JD020090, 2013.

Gautam, R., Hsu, N. C., and Lau, K.-M.: Premonsoon aerosol characterization and radiative effects over the Indo-Gangetic Plains: Implications for regional climate warming, Journal of Geophysical Research: Atmospheres, 115, https://doi.org/10.1029/2010JD013819, 2010.

620   Gautam, R., Hsu, N. C., Lau, K.-M., Tsay, S.-C., and Kafatos, M.: Enhanced pre-monsoon warming over the Himalayan-Gangetic region from 1979 to 2007, Geophysical Research Letters, 36, https://doi.org/10.1029/2009GL037641, 2009.

Giglio, L., Schroeder, W., Hall, J. V. and Justice, C. O.: MODIS Collection 6 Active Fire Product User's Guide, Revision C, NASA, 2020.

Gogoi, M. M., Babu, S. S., Moorthy, K. K., Bhuyan, P. K., Pathak, B., Subba, T., Chutia, L., Kundu, S. S., Bharali, C., 625   Borgohain, A., Guha, A., De, B. K., Singh, B., and Chin, M.: Radiative effects of absorbing aerosols over northeastern India: Observations and model simulations, Journal of Geophysical Research: Atmospheres, 122, 1132-1157, https://doi.org/10.1002/2016JD025592, 2017.

Gogoi, M. M., Jayachandran, V. N., Vaishya, A., Babu, S. N. S., Satheesh, S. K., and Moorthy, K. K.: Airborne in situ measurements of aerosol size distributions and black carbon across the Indo-Gangetic Plain during SWAAMI– 630   RAWEX, Atmos. Chem. Phys., 20, 8593-8610, https://doi.org/10.5194/acp-20-8593-2020, 2020.

Gogoi, M. M., Lakshmi, N. B., Nair, V. S., Kompalli, S. K., Moorthy, K. K., and Babu, S. S.: Seasonal contrast in the vertical profiles of aerosol number concentrations and size distributions over India: Implications from RAWEX aircraft campaign, Journal of Earth System Science, 128, 225, https://doi.org/10.1007/s12040-019-1246-y, 2019.

Gogoi, M. M., Moorthy, K. K., Sobhan Kumar, K., Jai Prakash, C., Babu, S. S., Manoj, M. R., Vijayakumar, S. N., and 635   Tushar, P. P.: Physical and optical properties of aerosols in a free tropospheric environment: Results from long-term observations over western trans-Himalayas, Atmospheric Environment, 84, 262-274, https://doi.org/10.1016/j.atmosenv.2013.11.029, 2014.

Gogoi, M. M., S, K, Manoj, M. R., and Jai Prakash, C.: Absorption characteristics of aerosols over the northwestern region of India: Distinct seasonal signatures of biomass burning aerosols and mineral dust, Atmospheric Environment, 73, 640   92-102, https://doi.org/10.1016/j.atmosenv.2013.03.009, 2013.

Gogoi, M. M., Babu, S. S., Arun, B. S. et al.: Response of ambient BC concentration across the Indian region to the nation-wide lockdown: Results from the ARFINET measurements of ISRO-GBP, Current Science, 120, 2, 341-351, https://doi.org/10.18520/cs/v120/i2/341-351, 2021.

GOSAT-2 TANSO-CAI-2 L2 Cloud Discrimination Processing Algorithm Theoretical Basis Document, National Institute 645   for Environmental Studies GOSAT-2 Project, NIES-GOSAT2-ALG-20191008-009-00, 2020.

Guha, A., De, B. K., Dhar, P., Banik, T., Chakraborty, M., Roy, R., Choudhury, A., Gogoi, M. M., Babu, S. S., and Moorthy, K. K.: Seasonal Characteristics of Aerosol Black Carbon in Relation to Long Range Transport over Tripura in Northeast India, Aerosol and Air Quality Research, 15, 786-798, https://doi.org/10.4209/aaqr.2014.02.0029, 2015.

Gustafsson, Ö. and Ramanathan, V.: Convergence on climate warming by black carbon aerosols, Proceedings of the 650   National Academy of Sciences, 113, 4243-4245, https://doi.org/10.1073/pnas.1603570113, 2016.

Hansen, A. D. A., Rosen, H., and Novakov, T.: The aethalometer — An instrument for the real-time measurement of optical absorption by aerosol particles, Science of The Total Environment, 36, 191-196, https://doi.org/10.1016/0048-9697(84)90265-1, 1984.

Hansen, A. D. A., Rosen, H., and Novakov, T.: The aethalometer — An instrument for the real-time measurement of optical absorption by aerosol particles, Science of The Total Environment, 36, 191-196, https://doi.org/10.1016/0048-9697(84)90265-1, 1984.

Hashimoto, M. and Nakajima, T.: Development of a remote sensing algorithm to retrieve atmospheric aerosol properties using multiwavelength and multipixel information, Journal of Geophysical Research: Atmospheres, 122, 6347-6378, https://doi.org/10.1002/2016JD025698, 2017.

Hersbach H., Bell, B., Berrisford P. et al.: The ERA5 global reanalysis. Quarterly Journal of Royal Meteorological Society, 146, 1999–2049, https://doi.org/10.1002/qj.3803, 2020.

Hsu, N. C., Jeong, M.-J., Bettenhausen, C., Sayer, A. M., Hansell, R., Seftor, C. S., Huang, J., and Tsay, S.-C.: Enhanced Deep Blue aerosol retrieval algorithm: The second generation, Journal of Geophysical Research: Atmospheres, 118, 9296-9315, https://doi.org/10.1002/jgrd.50712, 2013.

Hsu, N. C., Si-Chee, T., King, M. D., and Herman, J. R.: Aerosol properties over bright-reflecting source regions, IEEE Transactions on Geoscience and Remote Sensing, 42, 557-569, https://doi.org/10.1109/TGRS.2004.824067, 2004.

Hsu, N. C., Tsay, S., King, M. D., and Herman, J. R.: Deep Blue Retrievals of Asian Aerosol Properties During ACE-Asia, IEEE Transactions on Geoscience and Remote Sensing, 44, 3180-3195, https://doi.org/10.1109/TGRS.2006.879540, 2006.

IPCC, 2021: Climate Change 2021 - The Physical Science Basis. Contribution of Working Group I to the Sixth Assessment Report of the Intergovernmental Panel on Climate Change (Masson-Delmotte, V., P. Zhai, A. Pirani, S.L. Connors, C. Péan, S. Berger, N. Caud, Y. Chen, L. Goldfarb, M.I. Gomis, M. Huang, K. Leitzell, E. Lonnoy, J.B.R. Matthews, T.K. Maycock, T. Waterfield, O. Yelekçi, R. Yu, and B. Zhou (eds.)). Cambridge University Press, Cambridge, United Kingdom and New York, NY, USA, https://doi.org/10.1017/9781009157896.

Jayaraman, A., Satheesh, S. K., Mitra, A. P. and Ramanathan, V.: Latitude gradient in aerosol properties across the Inter Tropical Convergence Zone: Results from the joint Indo-US study onboard Sagar Kanya, Current Sci, 80, 10, 2001.

Justice, C. O., Kendall, J. D., Dowty, P. R., and Scholes, R. J.: Satellite remote sensing of fires during the SAFARI campaign using NOAA Advanced Very High Resolution Radiometer data, Journal of Geophysical Research: Atmospheres, 101, 23851-23863, https://doi.org/10.1029/95JD00623, 1996.

Kaufman, Y. J.: Satellite sensing of aerosol absorption, Journal of Geophysical Research: Atmospheres, 92, 4307-4317, https://doi.org/10.1029/JD092iD04p04307, 1987.

Kompalli, S. K, K., Babu, S. S., Moorthy, K. K., Manoj, M. R., Kumar, N. V. P. K., Shaeb, K. H. B., and Ashok Kumar, J.: Aerosol black carbon characteristics over Central India: Temporal variation and its dependence on mixed layer height, Atmospheric Research, 147-148, 27-37, https://doi.org/10.1016/j.atmosres.2014.04.015, 2014.

Kompalli, S. K., Babu, S. N. S., Moorthy, K. K., Satheesh, S. K., Gogoi, M. M., Nair, V. S., Jayachandran, V. N., Liu, D., Flynn, M. J., and Coe, H.: Mixing state of refractory black carbon aerosol in the South Asian outflow over the northern Indian Ocean during winter, Atmos. Chem. Phys., 21, 9173–9199, https://doi.org/10.5194/acp-21-9173-2021, 2021.

Kondo, Y., Sahu, L., Kuwata, M., Miyazaki, Y., Takegawa, N., Moteki, N., Imaru, J., Han, S., Nakayama, T., Oanh, N. T. K., Hu, M., Kim, Y. J., and Kita, K.: Stabilization of the Mass Absorption Cross Section of Black Carbon for Filter-Based Absorption Photometry by the use of a Heated Inlet, Aerosol Science and Technology, 43, 741-756, https://doi.org/10.1080/02786820902889879, 2009.

Lesins, G., Chylek, P., Lohmann, U.: A study of internal and external mixing scenarios and its effect on aerosol optical properties and direct radiative forcing, Journal of Geophysical Research, 107(D10), 4094, https://doi.org/10.1029/doi:10.1029/2001JD000973, 2002.

Levy, R. C., Remer, L. A., Mattoo, S., Vermote, E. F., and Kaufman, Y. J.: Second-generation operational algorithm: Retrieval of aerosol properties over land from inversion of Moderate Resolution Imaging Spectroradiometer spectral reflectance, Journal of Geophysical Research: Atmospheres, 112, https://doi.org/10.1029/2006JD007811, 2007.

Lyapustin, A., Wang, Y., Laszlo, I., Kahn, R., Korkin, S., Remer, L., Levy, R., and Reid, J. S.: Multiangle implementation of atmospheric correction (MAIAC): 2. Aerosol algorithm, Journal of Geophysical Research: Atmospheres, 116, https://doi.org/10.1029/2010JD014986, 2011.

Manoj, M. R., Satheesh, S. K., Moorthy, K. K., Gogoi, M. M., and Babu, S. S.: Decreasing Trend in Black Carbon Aerosols Over the Indian Region, Geophysical Research Letters, 46, 2903-2910, https://doi.org/10.1029/2018GL081666, 2019.

Martins, J. V., Artaxo, P., Liousse, C., Reid, J. S., Hobbs, P. V., and Kaufman, Y. J.: Effects of black carbon content, particle size, and mixing on light absorption by aerosols from biomass burning in Brazil, Journal of Geophysical Research: Atmospheres, 103, 32041-32050, https://doi.org/10.1029/98JD02593, 1998.

Nair, V. S., Babu, S. S., Gogoi, M. M., and Moorthy, K. K.: Large-scale enhancement in aerosol absorption in the lower free troposphere over continental India during spring, Geophysical Research Letters, 43, 11,453-411,461, https://doi.org/10.1002/2016GL070669, 2016.

Nair, V. S., Moorthy, K. K., Alappattu, D. P., Kunhikrishnan, P. K., George, S., Nair, P. R., Babu, S. S., Abish, B., Satheesh, S. K., Tripathi, S. N., Niranjan, K., Madhavan, B. L., Srikant, V., Dutt, C. B. S., Badarinath, K. V. S., and Reddy, R. R.: Wintertime aerosol characteristics over the Indo-Gangetic Plain (IGP): Impacts of local boundary layer processes and long-range transport, Journal of Geophysical Research: Atmospheres, 112, https://doi.org/10.1029/2006JD008099, 2007.

Nakajima, T., Yoon, S.-C., Ramanathan, V., Shi, G.-Y., Takemura, T., Higurashi, A., Takamura, T., Aoki, K., Sohn, B.-J., Kim, S.-W., Tsuruta, H., Sugimoto, N., Shimizu, A., Tanimoto, H., Sawa, Y., Lin, N.-H., Lee, C.-T., Goto, D., and Schutgens, N.: Overview of the Atmospheric Brown Cloud East Asian Regional Experiment 2005 and a study of the aerosol direct radiative forcing in east Asia, J. Geophys. Res., 112, D24S91, https://doi.org/10.1029/2007JD009009, 2007.

Park, R. J., Minjoong, J. K., Jaein, I. J., Daeok, Y., and Sangwoo, K.: A contribution of brown carbon aerosol to the aerosol light absorption and its radiative forcing in East Asia, Atmospheric Environment, 44, 1414-1421, https://doi.org/10.1016/j.atmosenv.2010.01.042, 2010.

Pathak, B., Kalita, G., Bhuyan, K., Bhuyan, P. K., and Moorthy, K. K.: Aerosol temporal characteristics and its impact on shortwave radiative forcing at a location in the northeast of India, Journal of Geophysical Research: Atmospheres, 115, https://doi.org/10.1029/2009JD013462, 2010.

Pathak, B., Subba, T., Dahutia, P., Bhuyan, P. K., Moorthy, K. K., Gogoi, M. M., Babu, S. S., Chutia, L., Ajay, P., Biswas, J., Bharali, C., Borgohain, A., Dhar, P., Guha, A., De, B. K., Banik, T., Chakraborty, M., Kundu, S. S., Sudhakar, S., and Singh, S. B.: Aerosol characteristics in north-east India using ARFINET spectral optical depth measurements, Atmospheric Environment, 125, 461-473, https://doi.org/10.1016/j.atmosenv.2015.07.038, 2016.

730 Prasad, P., M, M, Wei-Nai, C., S, Mukunda, M. G., Sobhan Kumar, K., K, and S: Characterization of atmospheric Black Carbon over a semi-urban site of Southeast India: Local sources and long-range transport, Atmospheric Research, 213, 411-421, https://doi.org/10.1016/j.atmosres.2018.06.024, 2018.

Ramnarine, E., Kodros, J. K., Hodshire, A. L., Lonsdale, C. R., Alvarado, M. J., and Pierce, J. R.: Effects of near-source coagulation of biomass burning aerosols on global predictions of aerosol size distributions and implications for 735 aerosol radiative effects, Atmos. Chem. Phys., 19, 6561-6577, https://doi.org/10.5194/acp-19-6561-2019, 2019.

Release Note: GOSAT-2 TANSO-CAI-2 L2 Aerosol Property Product, Product version 01.03, NIES-GOSAT2-SYS-20210310-019-00, 2021.

Sahu, S. K., Mangaraj, P., Beig, G., Samal, A., Pradhan, C., Dash, S. and Tyagi, B.: Quantifying the high-resolution seasonal emission of air pollutants from crop residue burning in India, Environmental Pollution, 286, 117165, 740 https://doi.org/10.1016/j.envpol.2021.117165, 2021.

Sand, M., Samset, B. H., Myhre, G., Gliß, J., Bauer, S. E., Bian, H., Chin, M., Checa-Garcia, R., Ginoux, P., Kipling, Z., Kirkevåg, A., Kokkola, H., Le Sager, P., Lund, M. T., Matsui, H., van Noije, T., Olivié, D. J. L., Remy, S., Schulz, M., Stier, P., Stjern, C. W., Takemura, T., Tsigaridis, K., Tsyro, S. G., and Watson-Parris, D.: Aerosol absorption in global models from AeroCom phase III, Atmos. Chem. Phys., 21, 15929-15947, https://doi.org/10.5194/acp-21-745 15929-2021, 2021.

Schuster, G. L., Dubovik, O., Holben, B. N., and Clothiaux, E. E.: Inferring black carbon content and specific absorption from Aerosol Robotic Network (AERONET) aerosol retrievals, Journal of Geophysical Research: Atmospheres, 110, https://doi.org/10.1029/2004JD004548, 2005.

Singh, A., Rajput, P., Sharma, D., Sarin, M. M., and Singh, D.: Black Carbon and Elemental Carbon from Postharvest 750 Agricultural-Waste Burning Emissions in the Indo-Gangetic Plain, Advances in Meteorology, 2014, 179301, https://doi.org/10.1155/2014/179301, 2014.

Suresh Babu, S., S. Nair, V., M. Gogoi, M., and Krishna Moorthy, K.: Seasonal variation of vertical distribution of aerosol single scattering albedo over Indian sub-continent: RAWEX aircraft observations, Atmospheric Environment, 125, 312-323, https://doi.org/10.1016/j.atmosenv.2015.09.041, 2016.

755 Torres, O., Ahn, C., and Chen, Z.: Improvements to the OMI near-UV aerosol algorithm using A-train CALIOP and AIRS observations, Atmos. Meas. Tech., 6, 3257-3270, https://doi.org/10.5194/amt-6-3257-2013, 2013.

Torres, O., Bhartia, P. K., Herman, J. R., Ahmad, Z., and Gleason, J.: Derivation of aerosol properties from satellite measurements of backscattered ultraviolet radiation: Theoretical basis, Journal of Geophysical Research: Atmospheres, 103, 17099-17110, https://doi.org/10.1029/98JD00900, 1998.

760 Torres, O., Bhartia, P. K., Herman, J. R., Sinyuk, A., Ginoux, P., and Holben, B.: A Long-Term Record of Aerosol Optical Depth from TOMS Observations and Comparison to AERONET Measurements, Journal of the Atmospheric Sciences, 59, 398-413, 10.1175/1520-0469(2002)059<0398:Altroa>2.0.Co;2, 2002.

Torres, O., Tanskanen, A., Veihelmann, B., Ahn, C., Braak, R., Bhartia, P. K., Veefkind, P., and Levelt, P.: Aerosols and surface UV products from Ozone Monitoring Instrument observations: An overview, Journal of Geophysical 765 Research: Atmospheres, 112, https://doi.org/10.1029/2007JD008809, 2007.

Vaishya, A, V., Prayagraj, S., Shantanu, R., and Babu, S. S.: Aerosol black carbon quantification in the central Indo-Gangetic Plain: Seasonal heterogeneity and source apportionment, Atmospheric Research, 185, 13-21, https://doi.org/10.1016/j.atmosres.2016.10.001, 2017.

Vaishya, A., Babu, S. N. S., Jayachandran, V., Gogoi, M. M., Lakshmi, N. B., Moorthy, K. K., and Satheesh, S. K.: Large contrast in the vertical distribution of aerosol optical properties and radiative effects across the Indo-Gangetic Plain during the SWAAMI–RAWEX campaign, Atmos. Chem. Phys., 18, 17669-17685, 10.5194/acp-18-17669-2018, 2018.

Vermote, E. F., Tanre, D., Deuze, J. L., Herman, M. and Morcette, J. J.: Second Simulation of the Satellite Signal in the Solar Spectrum, 6S: an overview, IEEE Transactions on Geoscience and Remote Sensing, 35, 3, 675-686, https://doi.org/ 10.1109/36.581987, 1997.

Vignati, E., Karl, M., Krol, M., Wilson, J., Stier, P., and Cavalli, F.: Sources of uncertainties in modelling black carbon at the global scale, Atmos. Chem. Phys., 10, 2595-2611, 10.5194/acp-10-2595-2010, 2010.

Wang, L., Li, Z., Tian, Q., Ma, Y., Zhang, F., Zhang, Y., Li, D., Li, K., and Li, L.: Estimate of aerosol absorbing components of black carbon, brown carbon, and dust from ground-based remote sensing data of sun-sky radiometers, Journal of Geophysical Research: Atmospheres, 118, 6534-6543, https://doi.org/10.1002/jgrd.50356, 2013.

Wang, R., Balkanski, Y., Boucher, O., Ciais, P., Schuster, G. L., Chevallier, F., Samset, B. H., Liu, J., Piao, S., Valari, M., and Tao, S.: Estimation of global black carbon direct radiative forcing and its uncertainty constrained by observations, Journal of Geophysical Research: Atmospheres, 121, 5948-5971, https://doi.org/10.1002/2015JD024326, 2016.

Wooster, M.J., Zhukov, B. and Oertel, D.: Fire radiative energy for quantitative study of biomass burning: derivation from the BIRD experimental satellite and comparison to MODIS fire products, Remote Sensing of Environment, 86, 1, 83-107, https://doi.org/10.1016/S0034-4257(03)00070-1, 2003.

Wooster, M. J. and Zhang, Y. H.: Boreal Forest fires burn less intensely in Russia than in North America, Geophysical Research Letters, 31, https://doi.org/10.1029/2004GL020805, 2004.

Soni, V.K., Pandithurai, G., Pai, D.S.: Evaluation of long-term changes of solar radiation in India. International Jouirnal of Climatology, 32 (4), 540–551, https://doi.org/10.1002/joc.2294, 2012.

Subba, T., Gogoi, M. M., Moorthy, K. K., Bhuyan, P. K., Pathak, B., Guha, A., Srivastava, M. K., Vyas, B. M., Singh, K., Krishnan, J., Lakshmikumar, T. V. S., Babu, S. S.: Aerosol Radiative Effects over India from Direct Radiation Measurements and Model Estimates, Atmospheric Research, 276, 106254, https://doi.org/10.1016/j.atmosres.2022.106254, 2022.

Dixon, R. K., Krankina, O. N.: Forest fires in Russia: carbon dioxide emissions to the atmosphere, Canadian Journal of Forest Research, 23, 700-705, 1993.

Leskinen, P., Lindner, M., Verkerk, P.J., Nabuurs, G.J., Van Brusselen, J., Kulikova, E., Hassegawa, M. and Lerink, B. (eds.).: Russian forests and climate change. What Science Can Tell Us 11. European Forest Institute, 2020.

Bao, F., Cheng, T., Li, Y., Gu, X., Guo, H., Wu, Y., Wang, Y., and Gao, J.: Retrieval of black carbon aerosol surface concentration using satellite remote sensing observations. Remote Sensing of Environment, 226, 93-108, 2019.

Bao, F., Li, Y., Cheng, T., Gao, J., and Yuan, S.: Estimating the Columnar Concentrations of Black Carbon Aerosols in China Using MODIS Products. Environmental Science & Technology, 54, 11025-11036, 2020.

Ceolato, R., Bedoya-Velásquez, A.E., Fossard, F. et al.: Black carbon aerosol number and mass concentration measurements by picosecond short-range elastic backscatter lidar. Scientific Report, 12, 8443, https://doi.org/10.1038/s41598-022-11954-7, 2022.

Hara, Y., Nishizawa, T., Sugimoto, N., Osada, K., Yumimoto, K., Uno, I., Kudo, R., Ishimoto, H.: Retrieval of Aerosol Components Using Multi-Wavelength Mie-Raman Lidar and Comparison with Ground Aerosol Sampling. Remote Sensing, 10(6):937. https://doi.org/10.3390/rs10060937, 2018.

810   Li, L., Che, H., Derimian, Y., Dubovik, O., Schuster, G.L., Chen, C., Li, Q., Wang, Y., Guo, B., & Zhang, X.: Retrievals of fine mode light-absorbing carbonaceous aerosols from POLDER/PARASOL observations over East and South Asia. Remote Sensing of Environment, 247, 111913, 2020.

Li, L., Dubovik, O., Derimian, Y., Schuster, G. L., Lapyonok, T., Litvinov, P., Ducos, F., Fuertes, D., Chen, C., Li, Z., Lopatin, A., Torres, B., and Che, H.: Retrieval of aerosol components directly from satellite and ground-based
815   measurements, Atmos. Chem. Phys., 19, 13409–13443, https://doi.org/10.5194/acp-19-13409-2019, 2019.

Nishizawa, T., Sugimoto, N., Matsui, I., Shimizu, A., Hara, Y., Itsushi, U., Kim, S.-W.: Ground-based network observation using Mie–Raman lidars and multi-wavelength Raman lidars and algorithm to retrieve distributions of aerosol components. Journal of Quantitative Spectroscopy and Radiative Transfer, 188, 79–93, 2017.

Wurl, D., Grainger, R. G., McDonald, A. J., and Deshler, T.: Optimal estimation retrieval of aerosol microphysical
820   properties from SAGE~II satellite observations in the volcanically unperturbed lower stratosphere, Atmos. Chem. Phys., 10, 4295–4317, https://doi.org/10.5194/acp-10-4295-2010, 2010.

Choi, M., Kim, J., Lee, J., Kim, M., Park, Y.-J., Jeong, U., Kim, W., Hong, H., Holben, B., Eck, T. F., Song, C. H., Lim, J.-H., and Song, C.-K.: GOCI Yonsei Aerosol Retrieval (YAER) algorithm and validation during the DRAGON-NE Asia 2012 campaign, Atmos. Meas. Tech., 9, 1377–1398, https://doi.org/10.5194/amt-9-1377-2016, 2016.
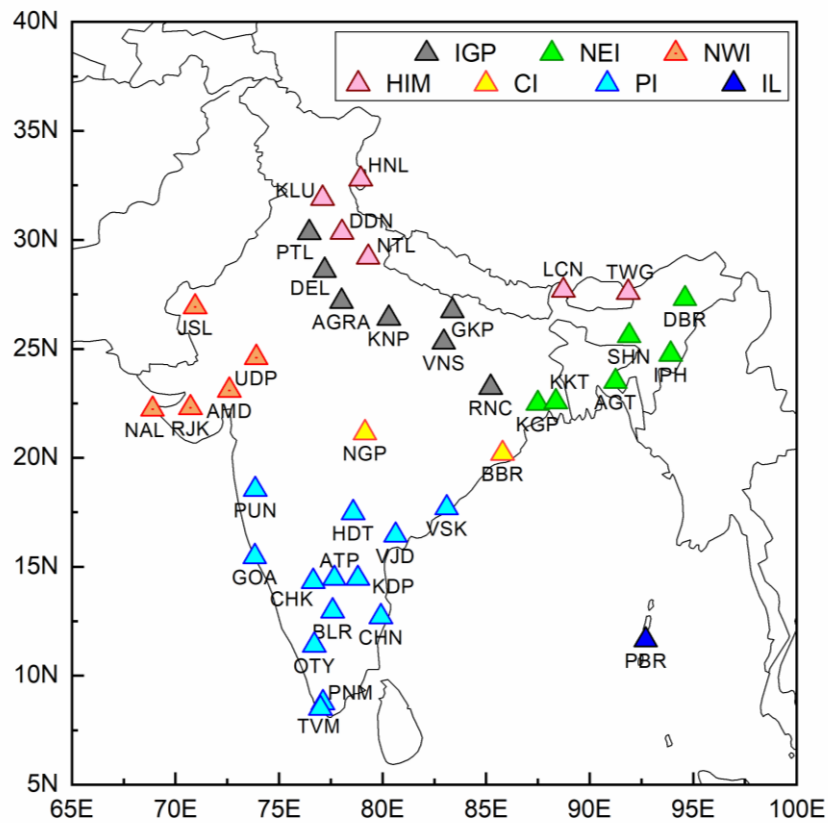
825

Figure-1: The network of aerosols observatories over India, distributed in the Indo-Gangetic Plains (IGP); North-eastern India (NEI); North-western India (NWI); Himalayan, sub-Himalayan and foothills regions (HIM), Central India (CI), Peninsular India (PI) and Island Locations (IL). More details about the ground-based observational locations in the ARFINET are provided in Supplementary Table-T1.
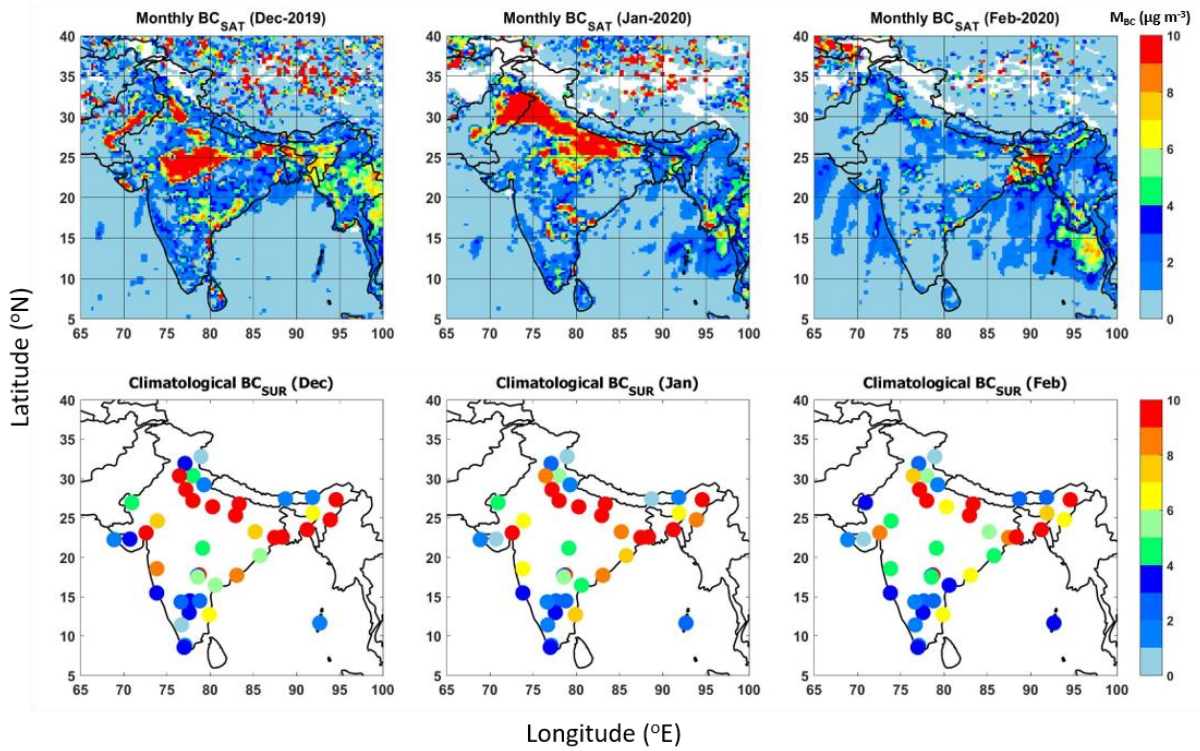
Figure 2: Regional distribution of monthly average BC over the Indian region from satellite (of the year 2019-2020) and surface measurements (climatological monthly average) during December-January-February (DJF) representing winter. The satellite-retrieved BC values (BC$_{SAT}$) are shown at 0.25 x 0.25 degrees spatial resolution. The surface BC (BC$_{SUR}$) in the bottom panel are climatological monthly average values at the point locations of the ARFINET. Minimum 3 to more than 10 years of data are included for the estimation of the climatological average. The color bars indicate the magnitudes of monthly average BC mass concentrations.
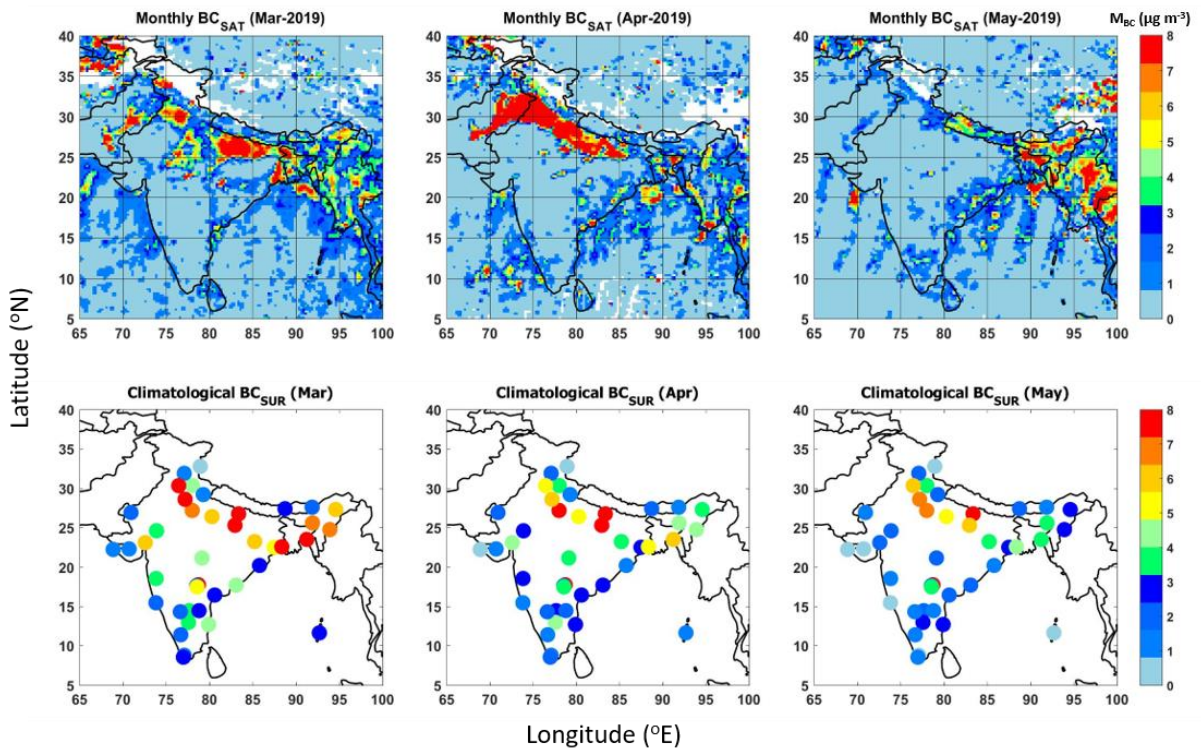
Figure 3: Same as Figure-2, for March-April-May (MAM), representing the pre-monsoon.

845
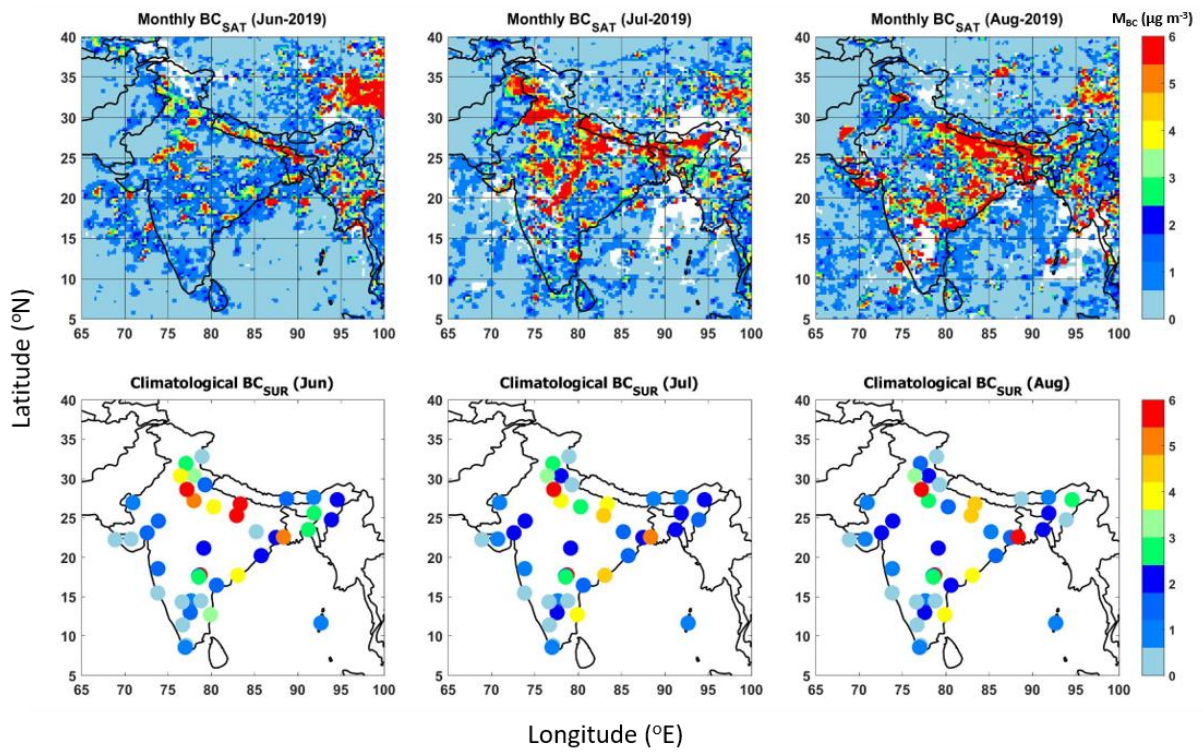
Figure 4: Same as Fig.2 and Fig.3 above, for June-July-August (JJA) representing monsoon.
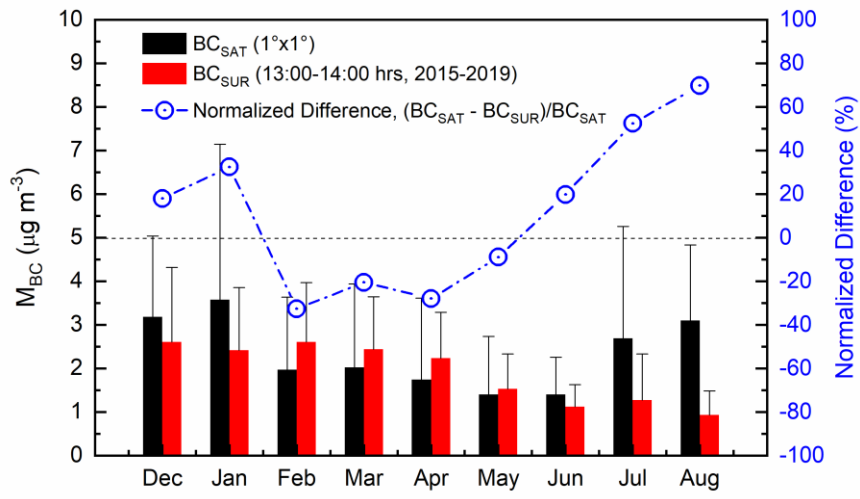
Figure 5: Monthly variation of the regional average values (averaged over all the locations considered for inter-comparison) of BC concentrations from satellite retrievals (BC$_{SAT}$) and surface measurements (BC$_{SUR}$), along with the normalized difference (in %) between the two data sets.
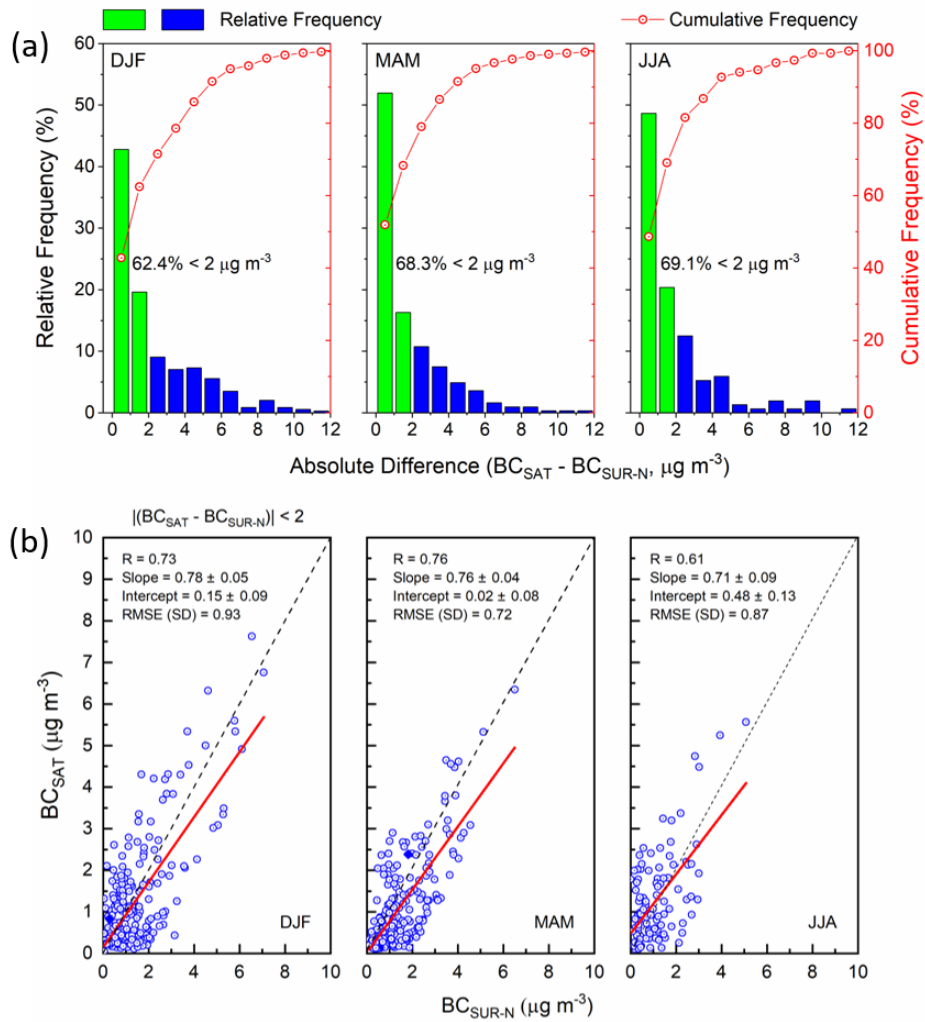
Figure 6: (a) Frequency counts (in percentage) of the absolute difference in BC (in μg m^{-3}) between simultaneous satellite (BC$_{SAT}$, averaged over 1 x 1-degree area around each of the ARFINET sites) and normalized surface BC (BC$_{SUR-N}$) concentrations; (b) Association between simultaneous satellite and normalized surface BC concentration. The solid red line is the linear fit, and the grey dash line is the one-to-one line of BC$_{SAT}$ and BC$_{SUR-N}$.
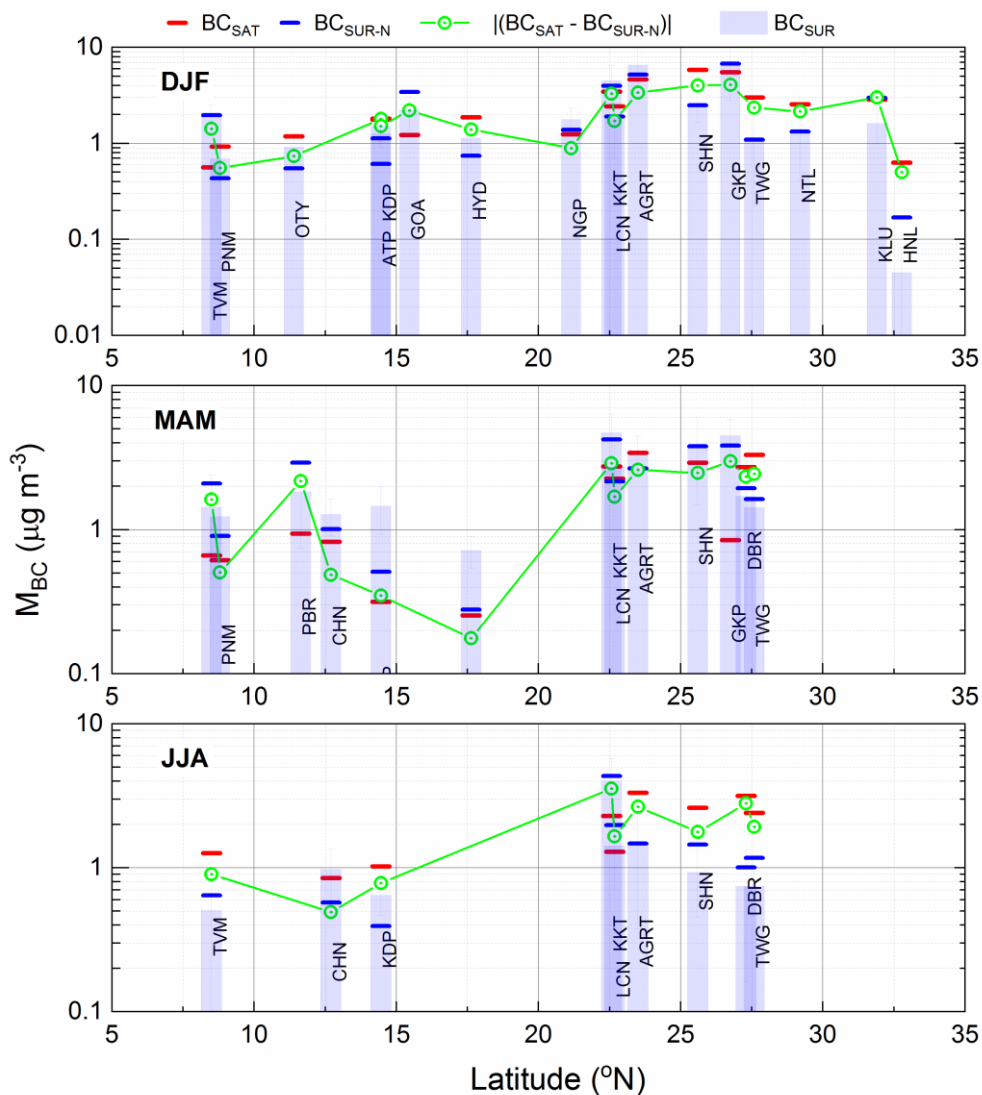
Figure 7: Seasonal mean values of satellite-retrieved (BC$_{SAT}$) and surface-measured (BC$_{SUR}$ and BC$_{SUR-N}$) BC concentrations at different ARFINET sites (shown with respect to their latitudes) of India. The absolute difference between BC$_{SAT}$ and BC$_{SUR-N}$ are also shown. The top panel shows the seasonal values of BC$_{SAT}$, BC$_{SUR}$, BC$_{SUR-N}$ and |(BC$_{SAT}$ - BC$_{SUR-N}$)| around each of the observational sites during December-January-February (DJF). Same parameters are shown in the middle panel for March-April-May (MAM) and bottom panel for June-July-August (JJA). The letters in the histograms represent the names of individual stations (details in supplementary Table-T1). The simultaneous data available for inter-comparison are highest in DJF (17-stations) and least in JJA (9-stations).
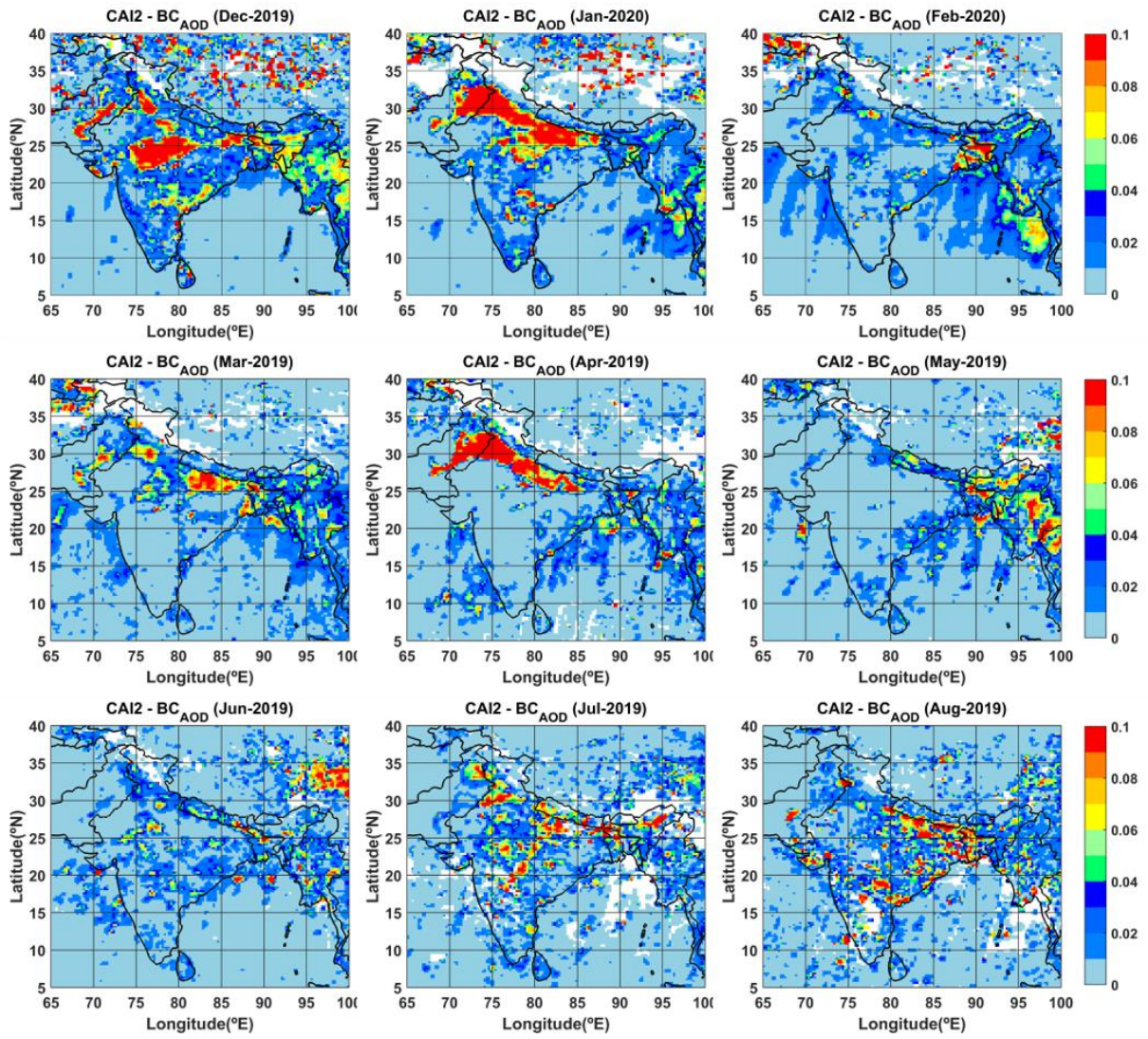
Figure 8: Regional distribution (0.25 x 0.25 degree) of monthly mean BC column optical depth (BC$_{AOD}$) over India during DJF, MAM and JJA of the years 2019-2020.
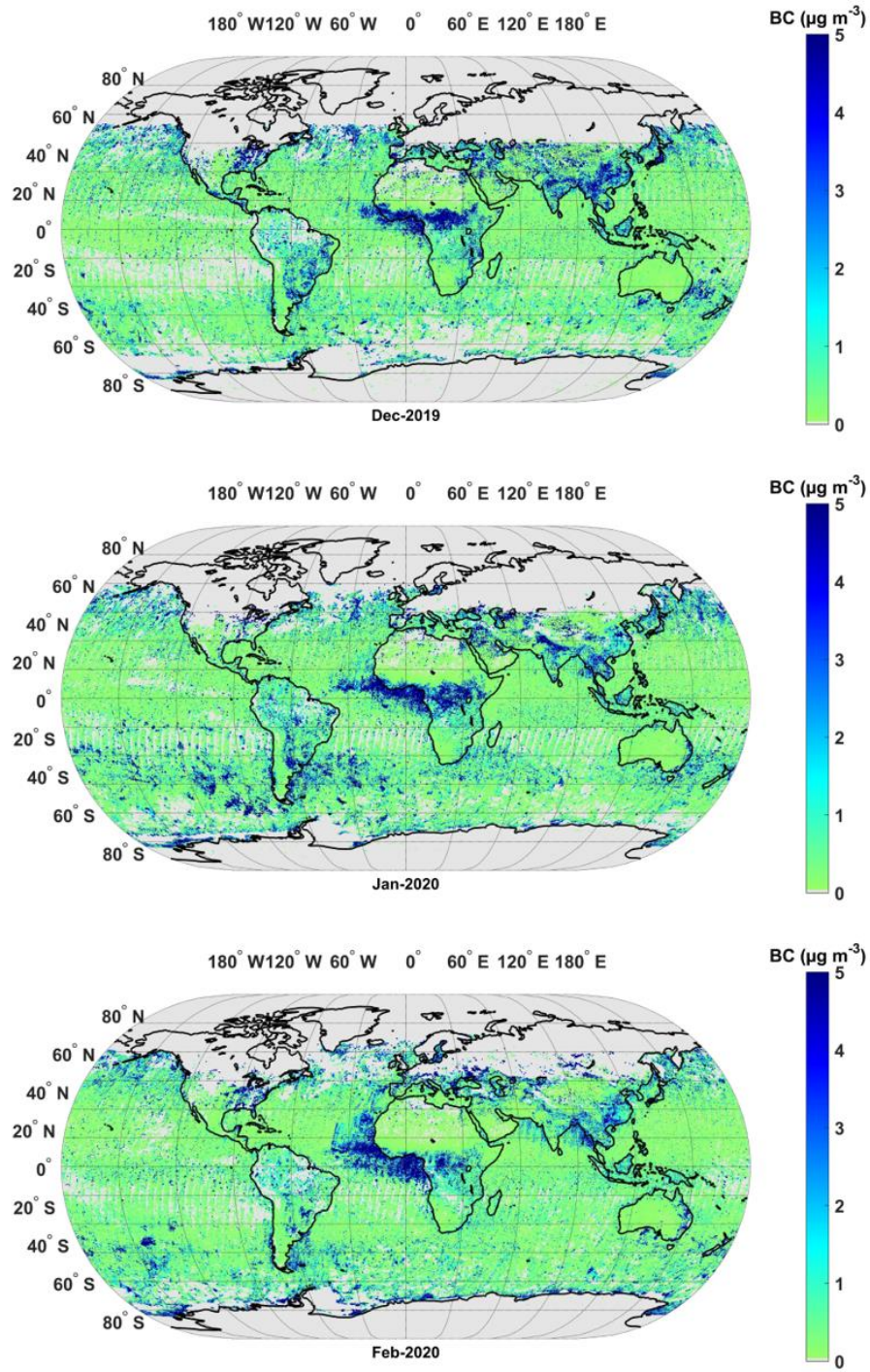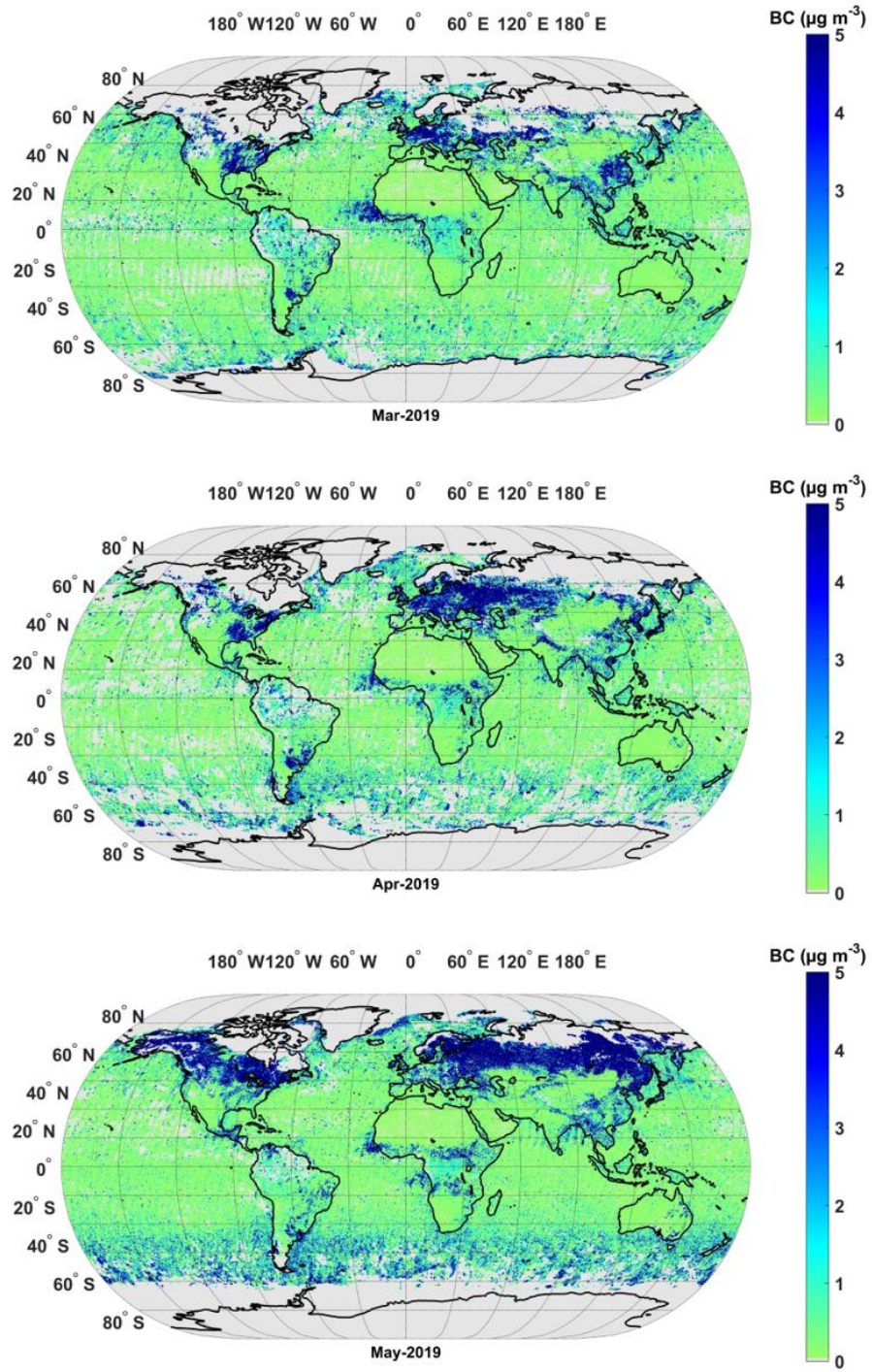
Figure 9: Global map of satellite retrieved BC (0.25 x 0.25 degree) during December (Dec-2019, top-panel) of the year 2019, and January (Jan-2020, middle-panel) and February (Feb-2020, bottom-panel) of the year 2020.

910

Figure 10: Global map of satellite retrieved BC (0.25 x 0.25 degree) during March (Mar-2019, top-panel), April (Apr-2019, middle-panel) and May (May-2019, bottom-panel) of the year 2019..
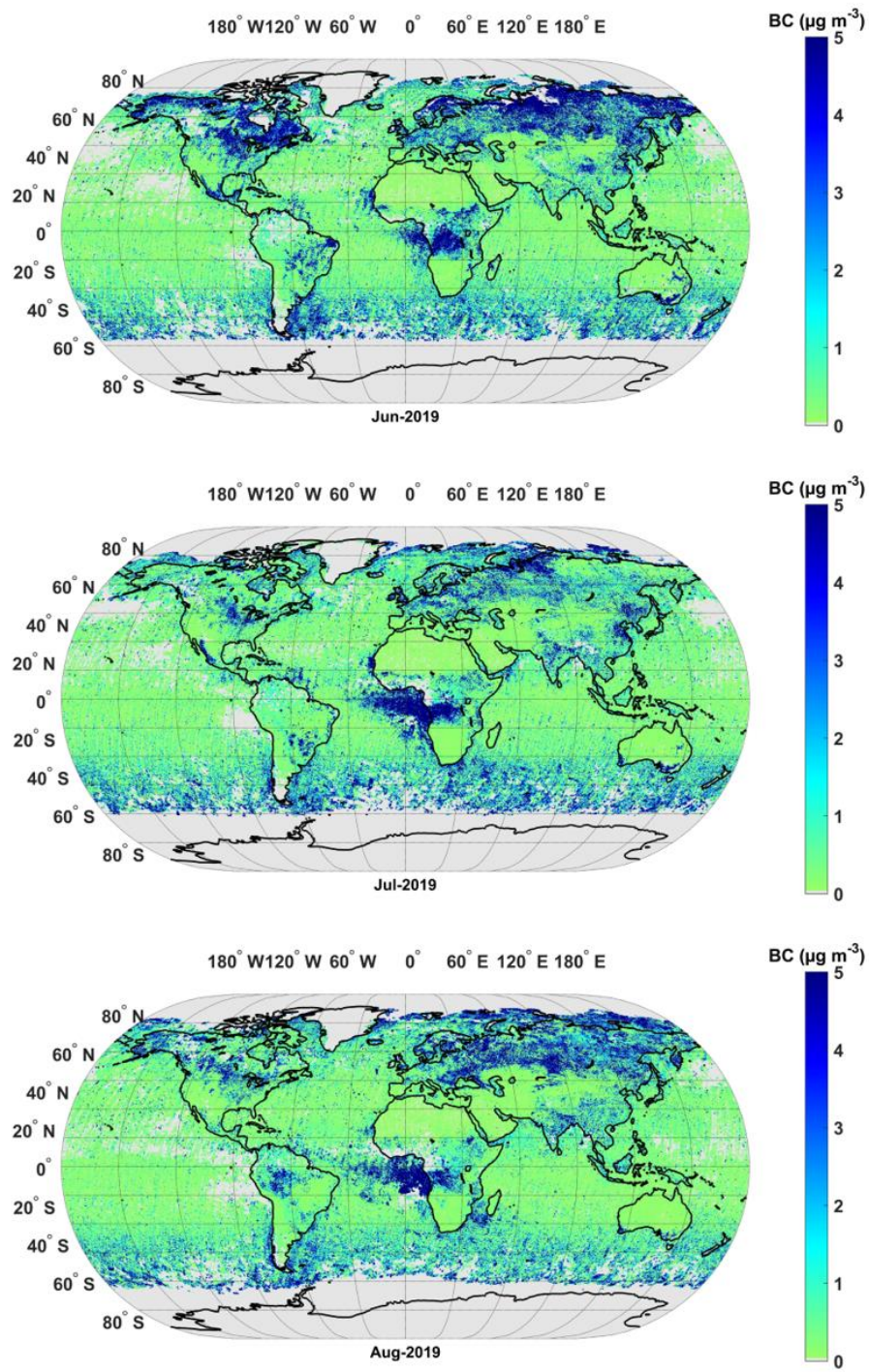
Figure 11: Global map of satellite retrieved BC (0.25 x 0.25 degree) during June (Jun-2019, top-panel), July (Jul-2019, middle-panel) and August (Aug-2019, bottom-panel) 0f the year 2019.

920

Table 1: Regional average BC over India from satellite and surface measurements. The satellite-based estimate is **made from 1 x 1 degree area average values around each of the ARFINET sites; while the climatological surface BC** **is for the period from 2015-2019 (13:00 to 14:00 hrs. local time).**

Period	Average BC over India ($\mu g\ m^{-3}$)		
	BC_{SAT}	BC_{SUR}	Normalized Difference (%)
DJF	2.91 ± 0.84	2.54 ± 0.11	12.7
MAM	1.72 ± 0.31	2.06 ± 0.47	-19.7
JJA	2.39 ± 0.89	1.11 ± 0.17	53.5